Exploration of turbulent separation over a CRM-HS model in a large scale wind tunnel

Ganesh Kumar Reddy Bommavaram

A thesis
submitted in partial fulfillment of the
requirements for the degree of

Master of Science

University of Washington

2024

Committee:

Owen J. H. Williams

Antonino Ferrante

Program Authorized to Offer Degree:
William E. Boeing Department of Aeronautics and Astronautics

University of Washington

Abstract

Exploration of turbulent separation over a CRM-HS model in a large scale wind tunnel

Ganesh Kumar Reddy Bommavaram

Chair of the Supervisory Committee:
Owen Williams
William E. Boeing Department of Aeronautics and Astronautics

The turbulent separated flow on a 4% High-Speed Common Research model (CRM-HS) configuration was studied using particle image velocimetry (PIV) in Kirsten Wind Tunnel (KWT) at the University of Washington without the nacelle/pylon group. The experiments were conducted for a range of Reynolds numbers and Angles of Attack (AOA) using tuft flow visualization to determine test conditions for PIV. The data is acquired in two configurations, namely side-on PIV and top-down PIV. In the side-on PIV, data is acquired in two fields of view (FoV) at three Reynolds numbers (Re = 5×10^5, 10^6, and 1.48×10^6) and three angles of attack (AoA) 10.5°, 12°, and 13.5° to explore the sensitivity of the separation region. In top-down PIV, data was acquired at two Reynolds numbers and one angle of attack (AoA) to explore the separation region along the wing span. A nominal case was set to a Reynolds number (Re) = 10^6 at AOA 12°. The separated flow in the nominal case didn't show reattachments on the wing surface. The boundary layer thickness increased with increasing angles at Re = (10^6), while the boundary layer thickness decreased with increasing Reynolds number at angle 12°. In top-down orientation, the flow is reversed near the wing surface in the streamwise direction and moves from root to tip in the spanwise direction. This experiment is the first step in designing the required hardware for the laser, camera mounts, and slides to enable PIV tests in a big-scale Kirsten wind tunnel facility. It also plays a key role in many upcoming tests on a more complex CRM-HL wing geometry

to acquire high-quality experimental data for CFD validation studies.

TABLE OF CONTENTS

Page

LIST OF FIGURES

LIST OF TABLES

NOMENCLATURE

α = Angle of attack

AoA = Angle of Attack

AR = Aspect ratio

c = Chord length at the side-on PIV location

Cref = Reference chord

Re = Reynolds number

Sref = Reference area

u' = Side-on PIV streamwise velocity fluctuations

u'_t = Top-down streamwise velocity fluctuations

U_c = Chord-wise mean streamwise velocity

U_t = Top-down mean streamwise velocity

$U\infty$ = Free-stream velocity

v' = Side-on PIV wall-normal velocity fluctuations

V_c = Chord-wise mean wall-normal velocity

w'_t = Top-down spanwise velocity fluctuations

W_t = Top-down mean spanwise velocity

Xref = Moment reference center x coordinate

x_c = Side-on PIV streamwise coordinates

x_t = Top-down PIV streamwise coordinates

Yref = Mean aerodynamic chord y coordinate

y_c = Side-on PIV wall-normal coordinates

Zref = Moment reference center z coordinate

z_t = Top-down PIV spanwise coordinates

λ = Taper-ratio

θ and $\wedge$ = Wing sweep angle

ACKNOWLEDGMENTS

I would like to thank my advisor Dr. Owen Williams for all this support and advice over these last two years. His constant feedback and patience have helped me learn a lot during this project. I want to especially thank him for the flexibility he provided during overwhelming times with academic work. His endless efforts and involvement in advising his students have impressed me with how much he is dedicated to research in this field.

I would like to thank all my lab colleagues for their feedback during lab meetings especially Alessandro Pulimeno, Kevin Manohar and Juanita Osoria Tovar who were involved in this project. I especially want to thank Alessandro Pulimeno for his support during the design and test phase of this project.

Last, but not least I would like to thank my family for all the continuous support they provided me to pursue this graduate degree. I would like to thank my friends especially Soumith Reddy and Varun Prakash who also continuously supported me with food throughout graduate school.

DEDICATION

To my family and friends

Chapter 1

INTRODUCTION

Scientists and engineers rely on Computational Fluid Dynamics (CFD) for analysing and predicting fluid behaviour. CFD predicts flow behaviour by solving fundamental governing equations, such as Navier-Stokes equations for variables like velocity, pressure, temperature, etc. In the engineering research and development process, CFD provides significant cost and time savings in comparison to physical wind tunnel and flight tests. However, these results from simulations must be validated with the experimental data to ensure accuracy in the design process. Although CFD solvers have been advanced in recent years, there are many known challenges. One of the largest of these challenges is the prediction of turbulent separated flows. In turbulent flows, only a few analytical solutions exist to Navier-Stokes equations because we end up with more unknowns than the number of equations while solving. To close this problem, CFD solvers make assumptions by introducing additional equations and empirical constants to approximate turbulence. A Direct Numerical Simulation (DNS) numerically solves the Navier-Stokes equations, however approach is computationally expensive. One widely used turbulence model in industries is the Reynolds Averaged Navier-Stokes (RANS) equation. This model describes the flow through Reynolds decomposition where the instantaneous flow variables are decomposed into their mean and fluctuating components, then averaging Navier-Stokes over time. Due to this time-averaged modelling, it can not capture the unsteadiness in the flow which provides details on the turbulent and boundary layer separations. This unsteadiness can be captured by the unsteady RANS (uRANS) model, which introduces the time dependency of RANS equations however, this model is also computationally expensive. The goal of this thesis is to explore the sensitivity of turbulent separated flows over a High-speed Common Research model (CRM-HS) using Particle Image Velocimetry (PIV) in a large-scale facility.

In 2014, NASA published a report on the CFD Vision 2030 study: A Path to Revolution-

ary Computational Aerosciences, which describes a path towards accurate CFD solvers[18]. This report presents the challenges of current state CFD tools to predict separated flows. Turbulent-separated flows play a key role in aerospace design applications which occur on airfoils, and wings which lead to reduced aerodynamic performance, increased drag, etc. Towards this vision, a High-Lift common research model (CRM-HL) wing geometry was introduced to focus on the separation and stall problems. To achieve this goal, they proposed to gather high-quality experimental data to validate CFD simulations. Obtaining validation quality data requires highly characterized and capable wind tunnel facilities as well as the use of multiple measurement techniques, emphasizing off-body, unsteady and turbulence measurements such as PIV. These latter measurements are not yet widespread in large-scale facilities commonly used for commercial testing and design of aircraft. The goal of this research is to perform PIV experiments in large-scale facilities and explore turbulent separation on CRM-HS configuration. This goal was achieved by conducting experiments using PIV in two orthogonal orientations in Kirsten Wind Tunnel (KWT), at the University of Washington. It is a commercial wind tunnel with a test section of 8 feet tall 12 feet wide and 10 feet long. We studied the sensitivity of the separation on the CRM-HS model undergoing stall, by looking at the turbulent velocity statistics.

To achieve this vision, a wide range of international groups have defined a series of standardized models to explore a range of aerodynamic phenomena, prediction and repeatability challenges. These include Reynolds number effects, wind tunnel model mounting systems constraints, differences in a wind tunnel and flight test model caused by design and manufacturing, and it requires careful designing of a slotted high-lift commercial wing due to balance contributions made by leading edge control surfaces, trailing-edge flaps during different phases on takeoff and landing [3]. To address these challenges, it was required to define standard models that will be tested in different wind tunnels to generate high-quality data sets for high-lift CFD validation. One such standardized model is a High Lift Common Research Model (CRM-HL) developed based on the High-Speed Common Research Model (CRM-HS), which was used for drag prediction workshops for CFD validation as a modern cruise wing design representing commercial aeroplane geometry. The CRM-HS was designed for high speeds and the CRM-HL was designed for low-speed purposes. This

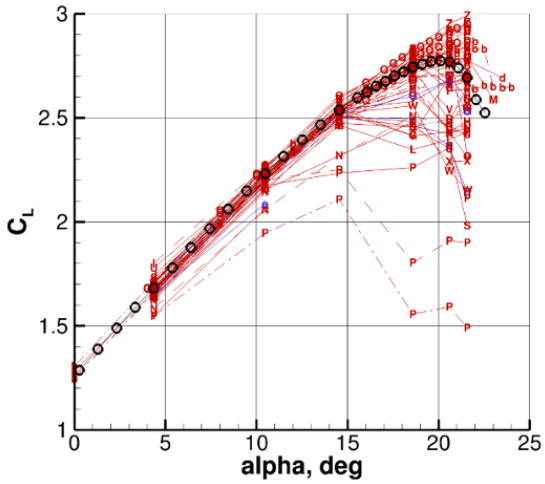

Figure 1.1: C_L prediction scatter plot from HLPW-3 [3]

high lift configuration included inboard and outboard leading edge slats and flaps to the CRM-HS to represent takeoff and landing positions. The leading edge slats and trailing edge flaps positions for a range of takeoff and landing conditions are defined in [4].

The CRM-HL is a modern, standard geometry wind tunnel model used to gather high-quality experimental wind tunnel test data for high-lift CFD validation efforts during High-lift prediction workshops (HLPW). These workshops are made publicly available to involve multiple partners in wind tunnel tests to ensure consistency in acquiring high-quality test data [3]. The interest in accurate CFD solvers is currently a great interest not only for improved aerodynamic performance but also for Certification by Analysis (CbA). A 2022, study published on the 20-Year Vision for Flight and Engine Certification by Analysis, also focuses on modelling technologies to overcome the costs associated with flight and engine development programs through Certification by Analysis to certify testing at lower costs while ensuring equivalent levels of safety [19]. Based on both of these interests a CRM-HL ecosystem has been established. This ecosystem includes HLPW's which provides a common database to enable direct comparison between CFD solvers and modelling approaches and also strengthens partnerships in enhancing CFD technology developments.

Until now, three workshops have been conducted, the HLPW-1 [15] focused on NASA

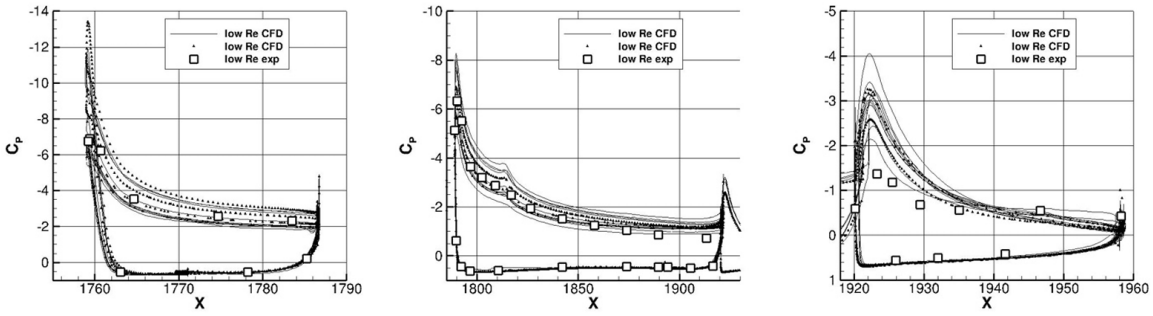

Figure 1.2: Wing tip Pressure coefficient distribution on the slat (left), main element (center), and flap (right) near $C_{L_{\max}}$ from HLPW-2 [3]

Trapezoidal Wing configuration [5], HLPW-2 [14] based on DLR-F11 configuration [13], and HLPW-3 [16] based on simplified CRM-HL [9] and JAXA standard model [3]. During these HLPW workshops, general and statistical analyses of computational results were presented by the participants. The main problem observed in computational results during these workshops is a large variation in lift ($C_{L,\max}$) at high angles of attack associated with flow separation presented in fig: 1.1. Running the computations with the same set of modelling assumptions has also shown large variations in the results[3]. These variations are thought to be due to different mesh resolutions, differences in implementing governing equations or differences in solution convergence. However, the statistical evidence over time suggested reduced variations of computational results at low angles of attack and large variations at high angles of attack. To address this challenge, the HLPW-2 and HLPW-3 workshop participants were requested to run RANS simulations only using the Spalart-Allmaras turbulence model and these results were able to match only up to 30% with the computational results suggesting errors in code implementation [3].

In HLPW-3, the results presented by Ito et al [6] have shown large variations between the wind tunnel test and RANS CFD solution during stall conditions. At these conditions the wind tunnel oil flow visualization tests have shown that the flow is mostly separated near the wing root and attached near the wing tip, however, most of the RANS computational results have shown a large separation at the wing tip and no separation near the wing

root. To explore this issue, they collected pressure coefficient data to highlight the regions where CFD was less accurate. From HLPW-2, it was known that from experiments, CFD predictions were inconsistent when the flow is separated near flaps and outboard the wing tip as shown in Fig:1.2. These figures are taken near the wing tip at $C_{L_{\max}}$. From Fig: 1.2 near the wing tip, all the computational data is inconsistent with the wind tunnel data. These observed differences between CFD prediction and wind tunnel data were thought to arise from many reasons, the first being that all the workshop participants were requested to run CFD simulations in free-air to compare to wind tunnel wall-corrected data rather than simulating the actual physical in-tunnel model and comparing directly with uncorrected test data. Second, they didn't account for the differences in the computational and wind tunnel models geometries [3]. Given the number of factors involved in these inconsistencies, the specific reasons remain unclear. To rectify this problem the overall goal of CRM-HL CFD validation studies has been broken down into smaller and more focused challenges to draw accurate conclusions.

Similar to CRM-HL, a CRM-HS wing geometry has also been developed, but with the goal of helping with drag prediction at cruise. This model is designed to test with and without the nacelle/pylon group. The results from this model were presented in the international AIAA CFD Drag Prediction Workshops (DPW) series, to improve numerical flow simulations for accurate drag and moments prediction. NASA's Subsonic Fixed Wing (SFW) Project within the Fundamental Aeronautics (FA) program established Technical Working Groups (TWG) to promote and coordinate CRM-HS development [21]. In January 2007, the SFW Aerodynamics TWG held their first meeting with technical leaders from Boeing, Lockheed-Martin, Northrop-Grumman, Gulfstream, Cessna, Hawker-Beechcraft, Pratt and Whitney, Air Force, Navy and NASA, to discuss a new experimental geometry to validate aerodynamic predictive tools [21]. The TWG designated that the CRM should be based on a transonic transport configuration designed to fly at Mach number M = 0.85 with a lift coefficient of C_L=0.5, and at Reynolds number Re = 40 million based on reference chord. The wing has an aspect ratio of AR=9.0 and a taper ratio of λ=0.275[21]. A detailed description of this geometry is presented in the methods section.

In order, to achieve the goals for a new set of high-quality experimental data NASA

has planned to test the CRM in the NASA Ames 11-ft transonic wind tunnel and the NASA National Transonic Facility (NTF) at Langley to acquire force, moment, surface pressure, and wing deformation in each facility. The NTF was set to acquire data at high Reynolds numbers and Ames to acquire skin friction and off-body data at low Reynolds numbers. In the Ames 11-ft transonic facility, the skin friction data was collected using a fringe imaging skin-friction interferometry (FISFI) and off-body data was collected by Particle Image Velocimetry (PIV) [21]. A similar set of experiments to compare tunnel-to-tunnel data variations was also conducted in the European Transonic Wind tunnel (ETW) that acquired force, moments, surface pressure, wing bending and twist, and surface flow visualization data [11]. Data was obtained at Reynolds number Re = 5×10^6 in all three wind tunnels, and Re = 19.8×10^6 and 30×10^6 in the NTF and ETW facilities. The NFT data showed a lower lift and higher drag value than the ETW and Ames. At Mach number M= 0.7, and three Reynolds numbers the NTF and ETW showed similar drag data, however at M= 0.85, the NTF drag data was 16 counts lower than the ETW data [11]. At Re = 5×10^6, the NTF pitching moment data was less nose down than ETW data and higher than Ames data. The surface pressures, wing bending and twist data were in good agreement between NTF and ETW data with some exceptions [11]. Dynamic data analysis on NASA's 80% CRM-HS model was conducted in JAXA wind tunnels [8]. In the current study, a similar experimental investigation is conducted within the Kirsten Wind Tunnel (KWT) at the University of Washington. In contrast to earlier CRM-HS studies, we focus on the stall characteristics of the model without the nacelle/pylon group and flow separation on the wing using PIV due to the availability of this model.

This thesis also leverages a recent study on the Gaussian Speed bump-separated flow geometry conducted at the University of Washington. This geometry was designed to study low-speed incompressible turbulent boundary layer separation over varying surface curvature and pressure gradients. This geometry is relevant to high-lift configurations with a thin incoming boundary layer over a larger curve [26]. PIV was acquired in two orthogonal planes, revealing both a separated shear layer and the shape of the separation [2] [7]. They looked at turbulent stress evolution over the surface. An example of this study is presented in Fig: 1.3 at $Re_L = 3.44 \times 10^6$ along y/L = 0.083.

This study features a CRM-HS configuration to explore the turbulent separated region using the PIV experimental approach to measure the flow fields for statistical analysis. The data is acquired in two configurations, namely side-on PIV and top-down PIV. In the side-on PIV, data is acquired at three Reynolds numbers and three angles of attack (AoA) to compare the separation region. In top-down PIV, data was acquired at two Reynolds numbers and one angle of attack (AoA) to explore the separation region along the wing span. This experiment is also a first step in designing the required hardware for the laser, camera mounts, and slides to enable PIV tests in a big-scale Kirsten wind tunnel facility. It also plays a key role in many upcoming tests on a more complex CRM-HL wing geometry to acquire high-quality experimental data.

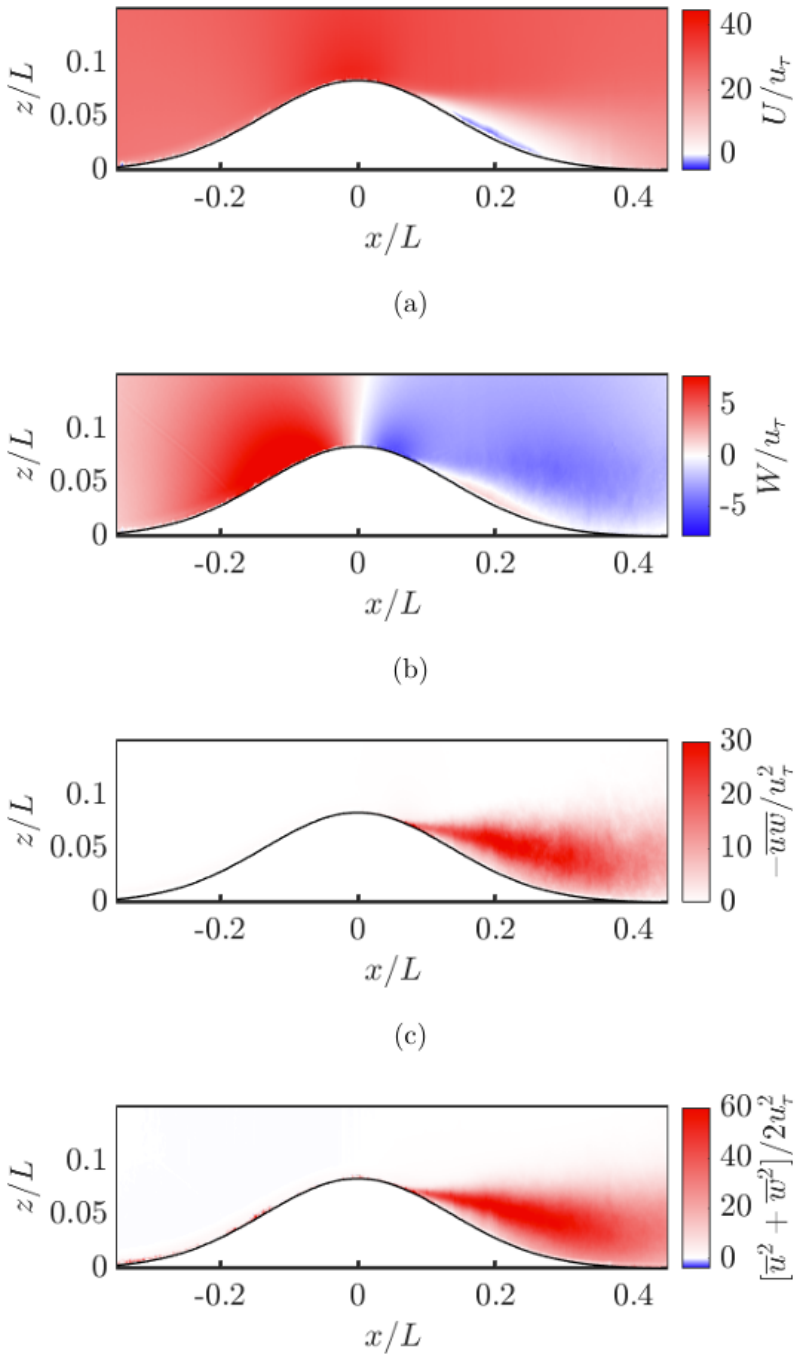

Figure 1.3: Mean (a) Streamwise velocity, (b) wall-normal velocity, (c) Reynolds shear stress, (d) and in-plane TKE along y/L = 0.083 at $Re_L = 3.44 \times 10^6$ [2]

Chapter 2

EXPERIMENTAL METHODS

2.1 Facility

All experiments were conducted in the subsonic Kirsten Wind Tunnel (KWT) at the University of Washington. This is a double-return, closed-circuit wind tunnel. The test section has a rectangular cross-section with 8 feet high, 12 feet wide and 10 feet long. It has 2 propellers with a 14 feet 9 inch-diameter, 7-blade fan driven by two 500-hp DC motors to provide airspeed ranging from 5 to 200 mph. These speeds provide dynamic pressures at about 0 psf to 100 psf (Pounds per square inch) for testing models in the wind tunnel. There are two vents 5 feet long and 2 inches wide located on the trailing edge walls of the test section to vent to the atmosphere and maintain the test section static pressure equal to the atmospheric pressure approximately [20].

The test article is mounted to the wind tunnel using a custom-designed 6-degree of freedom external side wall balance. The primary function of this side wall balance is to test large wing-only models and half models in KWT. A detailed list of capabilities and accuracy for the side wall balance is given in the KWT side wall balance technical guide [12]. The CRM-HS is mounted to the side wall balance through the mounting face shown in Fig: 2.3, to the west side of the test section. This tested CRM-HS geometry is 4% of full-scale. While the side wall balance was utilized to hold the model and was also undergoing testing, loads/moments data are not analysed in this thesis.

2.1.1 High-Speed Common Research Model (CRM-HS)

The high-speed common research model (CRM-HS) without the nacelle/pylon components that were used for the following experiments is shown in Fig:2.4. The CRM-HS geometry was designed to provide an experimental database to validate computational fluid dynamics (CFD) simulation results under high-speed cruise conditions. The international AIAA CFD

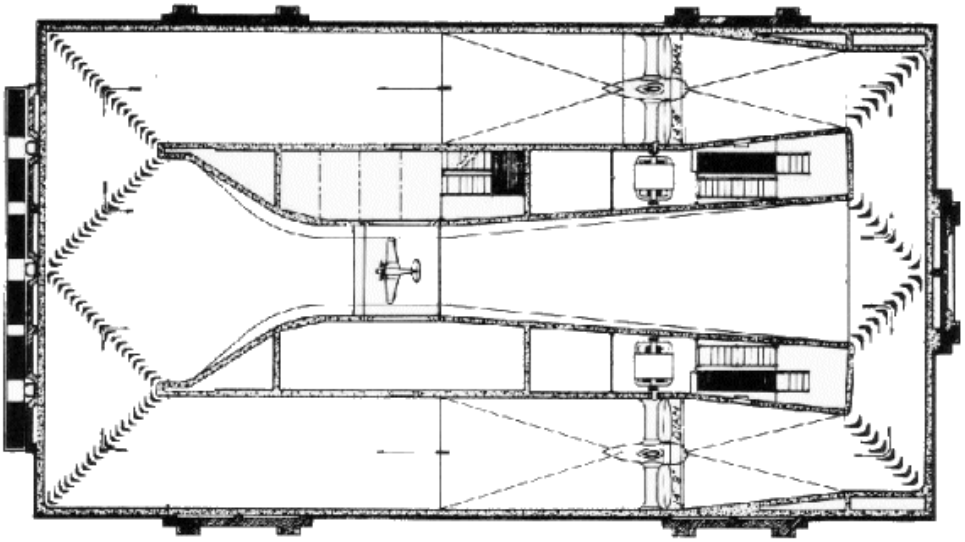

Figure 2.1: Top view of Kirsten Wind Tunnel.[20]

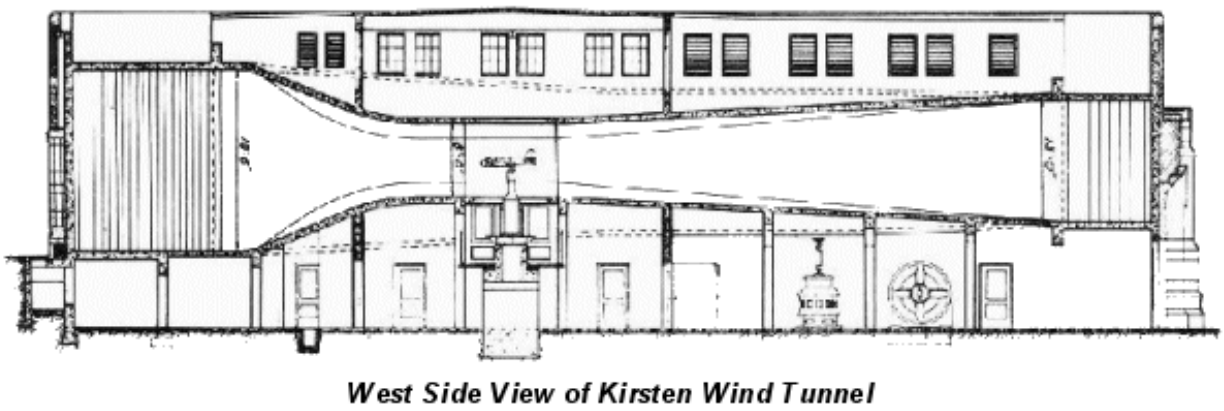

Figure 2.2: Left side view of Kirsten Wind Tunnel.[20]

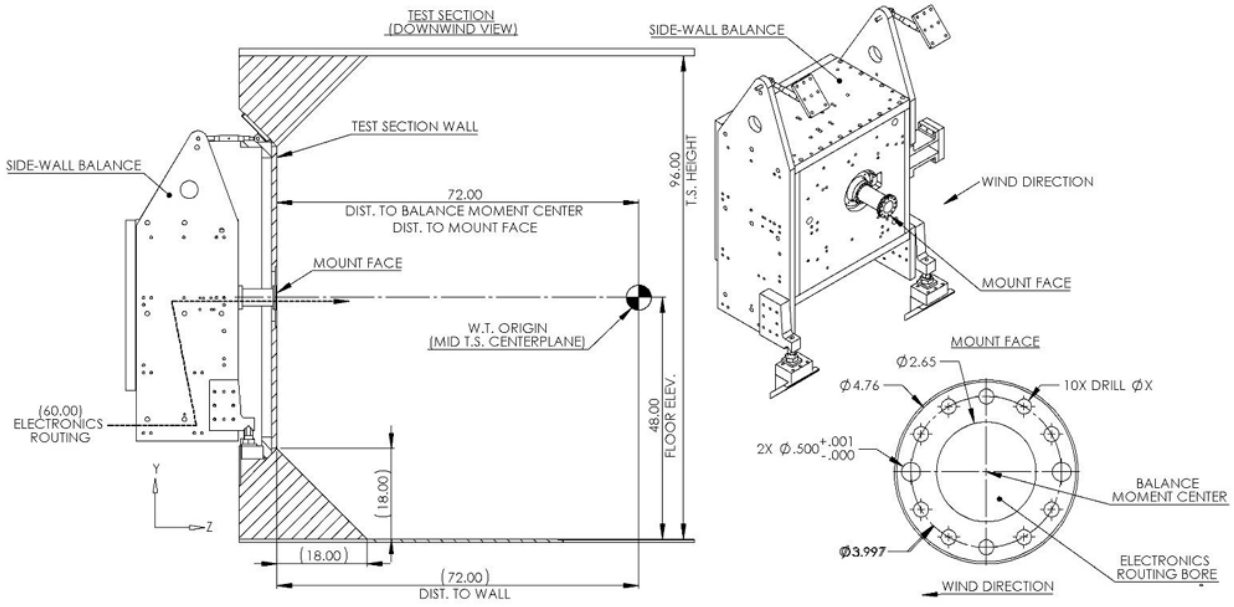

Figure 2.3: Side wall balance dimensions [12].

Drag Prediction Workshop (DPW) series organised by AIAA gathers high-quality experimental data to validate CFD results to improve numerical flow field simulations for accurate drag and moment predictions. NASA's Subsonic Fixed Wing (SFW) Project within the Fundamental Aeronautics (FA) Program has established a technical working group (TWG) to facilitate research and development within and outside NASA[21]. The TWG focused on a new high-speed wing model geometry to gather new experimental data based on DPW series[21]. This new configuration is known as the NASA High-speed Common Research Model (CRM-HS).

The TWG designated that CRM should be based on a transonic transport configuration designed to fly at Mach number M = 0.85 with a lift coefficient of C_L=0.5, and at Reynolds number Re = 40 million based on reference chord. The wing has an aspect ratio of AR=9.0 and a taper ratio of λ=0.275. Based on these values all the derived quantities for the full-scale model are presented in Table 2.1 and detailed geometric data for the CRM wing are provided in Fig [21]. Based on this data, the Boeing Company took the lead on the aerodynamic design, and the NASA FA/SFW Project took the lead on model design,

Table 2.1: Reference Quantities for the CRM [21]

Sref	594,720.0 in^2	4,130 ft^2
Trap-Wing Area	576,000.0 in^2	4,000 ft^2
Cref	275.80 in	
Span	2,313.50 in	192.8 ft
Xref	1,325.90 in	
Yref	468.75 in	
Zref	177.95 in	
λ	0.275	
$\wedge_{C/4}$	35°	
AR	9.0	

fabrication and testing of this CRM wing model [21].

2.2 Flow visualization

To determine testing conditions for subsequent PIV interrogation we performed flow visualization using mini tufts on the wing surface. The tufts were glued to the wing surface and had a circular cross-section of T41 (0.23 mm) and 12.7 mm (0.5 inches) long with a spacing of 25.4 mm (1 inch) in both span-wise and chord-wise directions starting about an inch from the leading edge. The tufts were made from Trilobal Florescent Polyester and glued with Duco cement thinned with acetone.

Once the nominal flow conditions were reached at each interval (10 seconds), the video was recorded for 34 seconds to capture the tuft motion. These videos were then processed into ensemble images for flow behaviour. First, the images were converted into greyscale and subtraction was applied by shifting images a single time step forward, to take the difference between the original unshifted images at each time step [22]. Applying subtraction removes most of the steady-state background from images while tracking the unsteadiness of tufts.

Tests were conducted tests at three Reynolds numbers, 5×10^5, 10^6 and 1.48×10^6

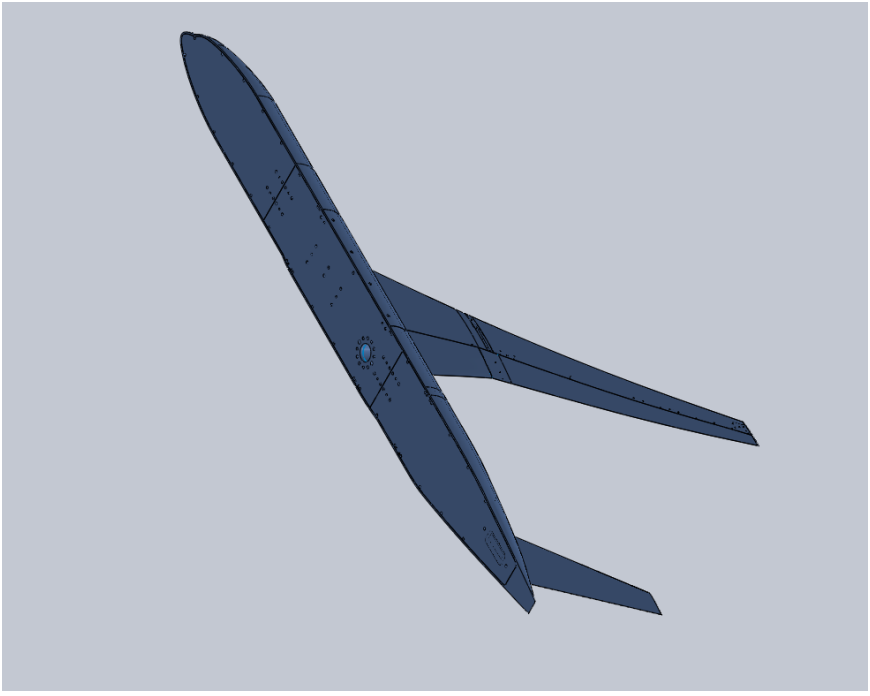

Figure 2.4: CRM-HS CAD model.

which correspond to 25.01, 50.01 and 74 m/s respectively, at different angles of attack at 1.5-degree intervals from -3 to 20 degrees to record tufts deflections. The Reynolds number was calculated using the mean aerodynamic chord, which is equivalent to 0.3 meters. Using this flow visualisation we were looking for a separated flow to determine the test conditions for subsequent PIV measurements.

Pulimeno ([1]) gives a more detailed summary of the tufting results. It was determined that flow separation could be seen near the wing tip at all three Reynolds numbers at angles 10.5, 12 and 13.5 degrees. An example of the tufting flow visualization output at AOA 12° and a Reynolds number of 10^6 is shown in Figure 2.5. From Fig 2.5, we can see the attached flow near the root of the wing and the separated flow in the spanwise direction towards the tip as marked. It was also found at Re = 10^6 with increasing AoA from 10.5° to 13.5° the flow separation moved towards the root of the wing [1]. At Re = 5×10^5, tufts visualization implied a partial reattachment zone even at higher AoA, and at highest Re = 1.67×10^6 the

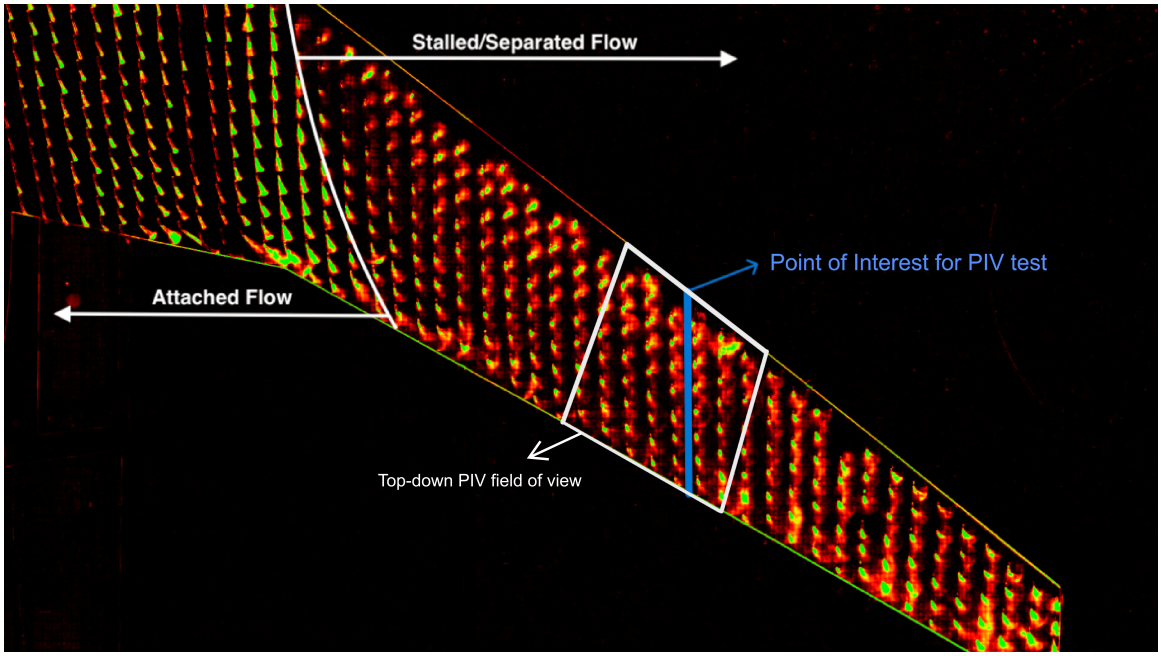

Figure 2.5: Video processed image with PIV illumination region at 12°and Re = 10^6.

wind tunnel was killed at AoA 10.5° due to tufts coming off the surface[1]. These results from flow visualization set our testing conditions to perform PIV experiments to study flow separation over the High-Speed Common Research Model (CRM-HS). Due to weaker separation and partial reattachment zone at low Re and lack of sufficient data at higher Re, a nominal PIV conditions was set at Re = 10^6 and AoA 12°. To explore the sensitivity of the separation, data was also acquired 1.5° on either side of 12° and at Reynolds number of 5×10^5 and 1.48×10^6. The location for the PIV experiment was chosen to be approximately 17 inches from the tip of the wing as shown in Fig:2.5. The chord length at this location is 193 mm (7.6 inches).

2.3 PIV setup

Particle image velocimetry (PIV) measurements offer a non-intrusive method of exploring the unsteady flow field over the wing. Instantaneous flow fields were obtained using a planar, double-exposure PIV. This setup uses one camera to capture the location of seeded particles

illuminated by the pulsating laser in quick succession. By cross-correlating these image pairs with the time known between the frames instantaneous velocity fields are obtained. To set up the PIV equipment in the wind tunnel, we had to come up with a new flexible design to hold and mount the laser and cameras as needed. A flexible design enables us to move the laser and cameras to any specific location on the test model. We designed laser and camera mounts for both orientations as detailed below. Using the PIV experimental approach is a challenge in a big facility due to a decrease in laser intensity as distance increases. When the distance is far from the laser head to the test model, the illuminated particles are not well captured in this region resulting in some bad vectors.

To study the dynamics of flow separation in streamwise and spanwise directions PIV experiment was performed in two orientations. One orientation is side-on PIV which highlights the separated shear layer and the second orientation is top-down PIV which gives spanwise flow dynamics. The orientation of both the fields of view relative to the wing surface is shown in Fig2.5. The side-on PIV setup is shown in Fig: 2.6 and the top-down PIV setup is shown in Fig: 2.7. In both of these images, the tunnel's right side walls are hidden to highlight the view of the camera and laser represented in blue lines and green laser sheets respectively.

For the side-on PIV orientation, the laser is placed on top of the wind tunnel test section to emit a high-energy laser sheet and the camera is placed on the tunnel side wall, perpendicular to the laser sheet. In this configuration, the laser can move to different spanwise locations on the wing surface by moving the traverse on top of the test section in the Y tunnel coordinates. A CAD model of this configuration is shown in Fig 2.8. A laser mount plate was designed to hold the laser in position and this plate was bolted into the traverse support as indicated in the figure. A flexible camera support beam was also designed to hold cameras to the same traverse support, this beam is designed to move 0.45 meters (1.5 feet) towards and away from the laser as required. The cameras can also slide along the support beam to adjust the distance from the laser sheet. A challenge during this design was with the distance of the camera support beam as we require a long distance to keep the camera angle less than 60° for an accurate camera view, but this was limited by the wind tunnel traverse design. This challenge was resolved by setting the camera view angle to 60°,

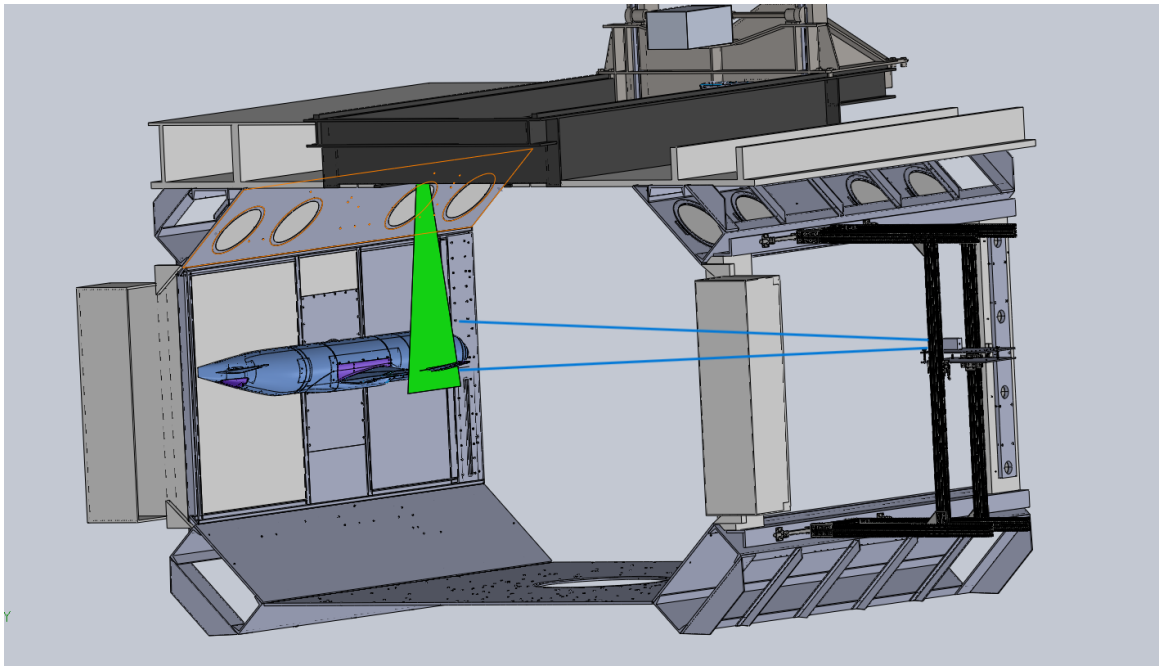

Figure 2.6: Side-on PIV CAD.

which gave us a distance of 1.6 meters for the camera support beam. Data was acquired at two regions, one near the trailing edge and another at the leading edge of the wing with an overlap of 86%. The fields of view for this orientation and their overlap are detailed in Fig: 2.9. In this configuration, all the data was acquired at 12° chordwise coordinates defined as x_c and y_c, where x_c are streamwise coordinates and y_c are wall-normal coordinates.

For the top-down orientation, the laser is placed on the side of the wind tunnel test section and the camera is placed on top of the test section to capture the scattered light. In this orientation, the laser sheet is approximately tangent to the surface of the wing and aligned with the chord as shown in Fig: 2.7. The laser sheet was within 5 mm from the surface. For this orientation, we designed a separate frame Fig: 2.10, that allows the laser head to move up, down, left, right, forward and backward to point the laser in the field of interest as needed for different angles of attack. This frame also holds the camera for side-on PIV orientation. A challenge we faced during this design was to design a frame that didn't block the test section door access. To resolve this we took the clearance distance of

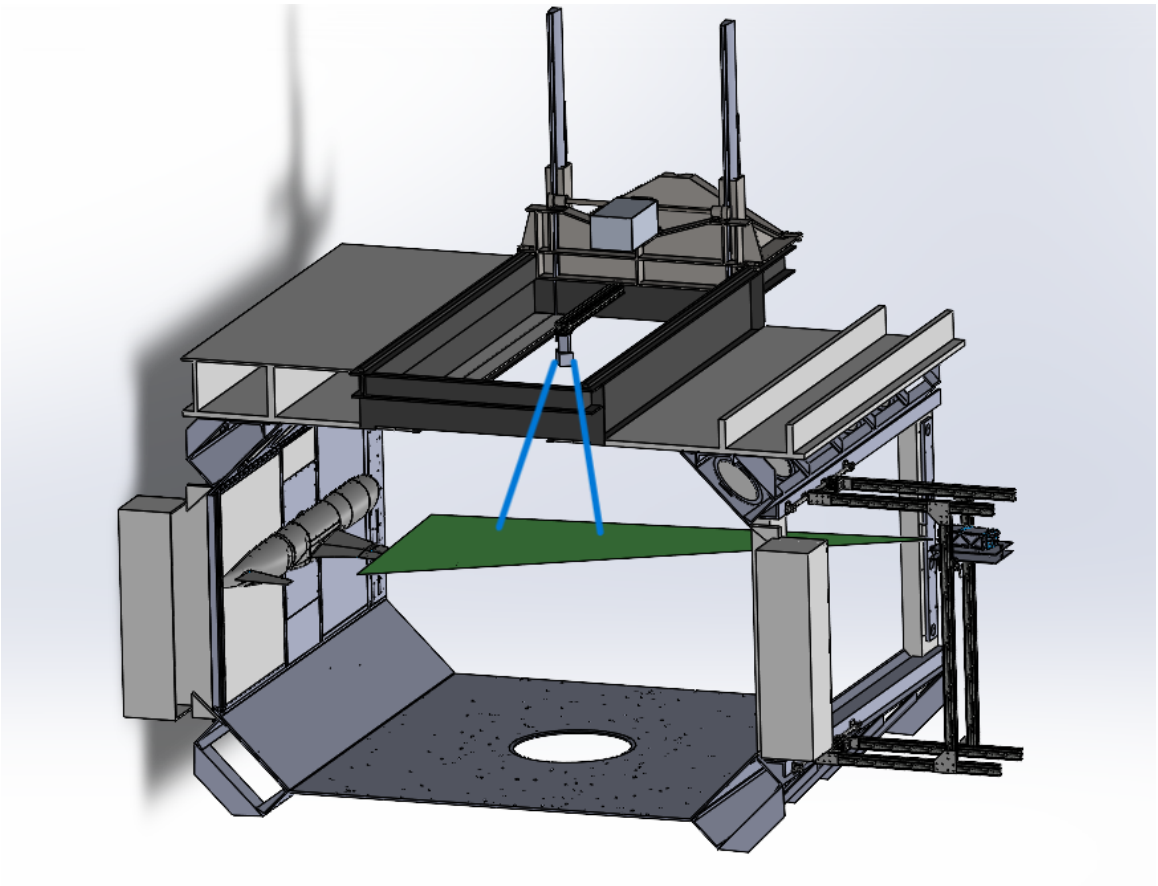

Figure 2.7: Top-down PIV CAD.

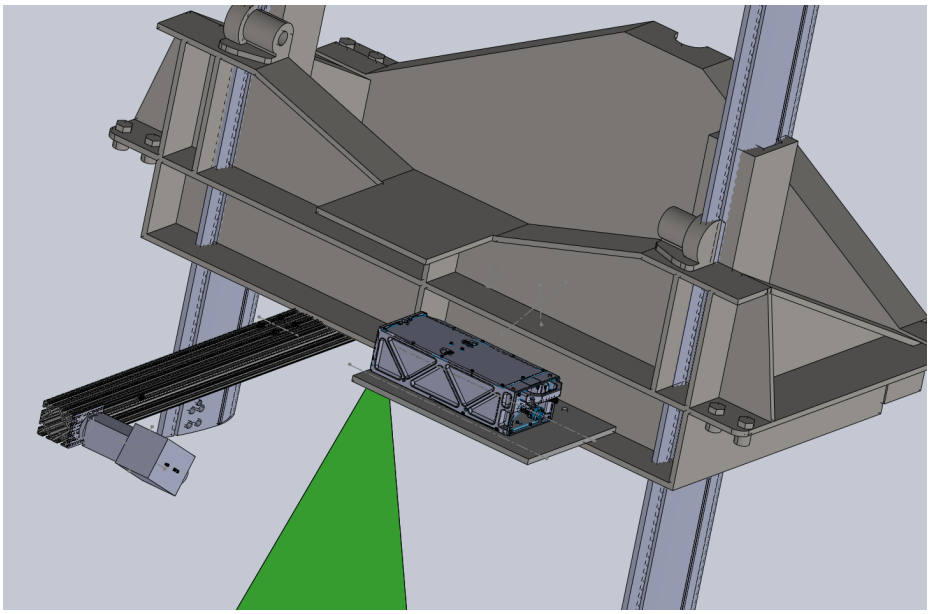

Figure 2.8: Side-on traverse CAD design.

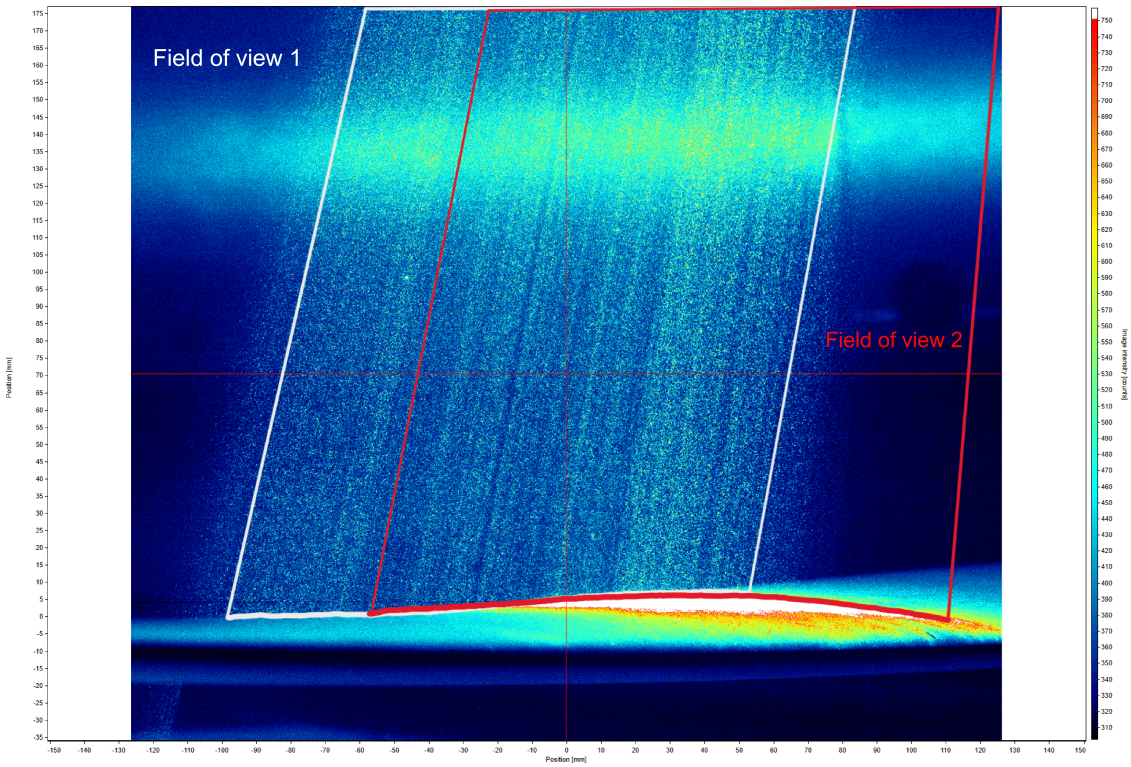

Figure 2.9: Frame 1 and frame 2 regions with 86% overlap.

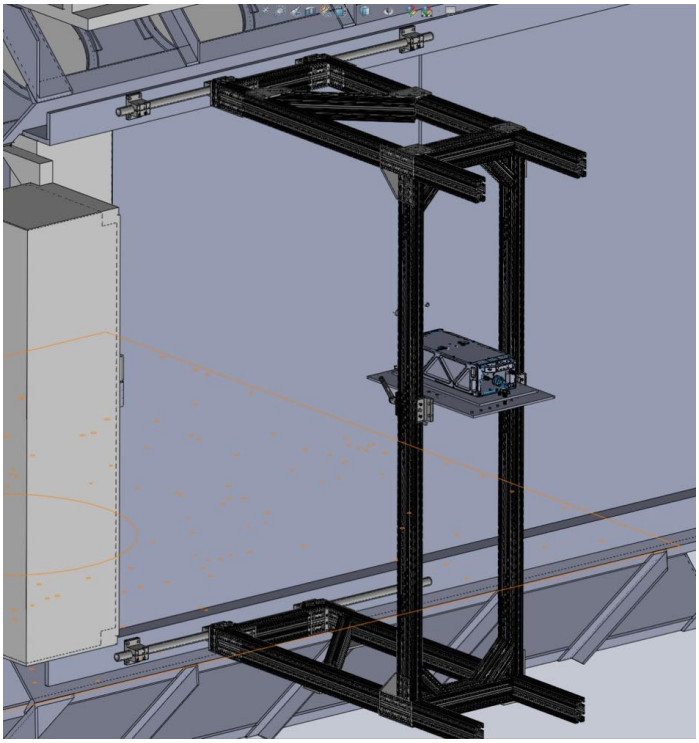

Figure 2.10: Top-down laser orientation and camera frame CAD design.

the door opening and designed the frame around it which allows access into the test section without any disturbance to the frame. As the wing has a small 5° dihedral angle the laser sheet distance from the surface varied from root to tip, but at the point of interest, it is within 5 mm from the surface. The centre of this field of view (FoV) is approximately at the spanwise location of the side-on PIV field of view and the orientation is parallel to the chord. The coordinates are defined as x_t and z_t, where x_t are streamwise coordinates and z_t are spanwise coordinates.

For the PIV experiment, the interior of the test section was seeded with DEHS smoke particles using the LaVision Aerosol generator. This smoke generator has 4 nozzle jets which produce 10^8 particles/second for each jet.

A single 5.5-megapixel Imager scientific sCMOS camera was used to capture the images. This camera sensor has a resolution of 2560 × 2160 pixels with a pixel size of $6.5 \times 6.5 \mu m^2$. For the side-on PIV, the field of view (FoV) of 250 by 210 mm (9.85 by 8.27 inches) was

captured using a Nikon 300 mm lens at $f/12$ aperture. For the top-down PIV, the FoV was 386 by 327 mm (15.23 by 12.9 inches) captured by a Nikon 60 mm lens at $f/8$ aperture.

The smoke particles were illuminated by a Quantel EverGreen 200mJ/pulse dual-pulsed Nd: YAG laser at a wavelength of 532 nm and 15 Hz reputation rate. The laser beam was released out of the laser head's aperture and directed 90 degrees downwards at the wing surface for side-on PIV and released parallel for the top-down PIV. The wing surface was applied with a black vinyl wrap film to reduce reflections off the surface. The film is a 2080 series made by 3M and was applied as per manufacturer instructions. This laser beam is then passed through adjustable optics to diverge the beam into a thin laser sheet of 2mm thickness.

The camera is focused on the sheet of the laser sheet using a calibration target. The calibration target used is a dual-plane LaVision Type 204-15 which has dimensions of 204 by 204 mm. The calibration target consists of a grid of squares, circles and triangles, that are automatically detected by the Davis LaVision software to recognize the calibration orientation. The resulting scaling factors are 10.12 pixels/mm for the side-on PIV and 6.6 pixels/mm for the top-down PIV.

2.3.1 PIV Data Acquisition

The PIV data acquisition was performed using the Davis 10 LaVision software. The first data set was obtained for the side-on PIV orientation for two fields of view (FoV). The second FoV was moved 24 mm towards the leading edge and 5 mm upwards from the first FoV. A total of 3000 frames were captured at 15 Hz frequency for Re = 10^6 at 10.5°, 12°. and 13.5°, while 1500 frames were captured at Re = 5×10^5 and 1.48×10^6 at 12° angle.

For the top-down configuration, data was acquired at 12° angle of attack for Re = 5×10^5 and 10^6. A total of 3000 frames were captured at Re = 10^6 and 1500 frames at Re = 5×10^5 with a maximum laser frequency of 15 Hz. The time between the frames is determined by restricting the maximum particle displacement to be within 16 pixels. The time between the laser pulse with respective velocity and Reynolds numbers for both configurations is shown in Table 2.2. In this configuration, we do not have the same test conditions as

Configurations	**Reynolds Number (Re)**	**Velocity (m/s)**	**dt** (μs)
Side-on PIV FoV 1, 2	5×10^5	25.01	47
	10^6	50.01	24
	1.48×10^6	74	16
Top-down PIV	5×10^5	25.01	80
	10^6	50.01	40

Table 2.2: Time between image pairs dt(μs), at corresponding Re and velocity (m/s) for two configurations

side-on PIV due to model shifting during testing. As the laser sheet was aligned with the nominal condition of 12° angle at Re = 10^6, we were able to collect data below this angle and Reynolds number. When the angle was above 12° the laser sheet was blocked by the wing surface and a similar case was also absorbed at 10.5°. When the Reynolds number was increased to Re = 1.48×10^6, the wing model was deflected by the dynamic pressure of the incoming flow resulting in blockage of the laser sheet.

2.3.2 PIV Processing

All the images were processed in the Davis 10 software. The first step of pre-processing was to stabilize the images due to vibrations from the wind tunnel and test article. For the side-on orientation, these images were passed through a subtraction time filter to remove the steady-state background with a filter length of 45 images. For the top-down orientation, the Butterworth high pass filter appeared to give a better background subtraction with a filter length of 45 images. Masking was done to remove regions of high light reflection intensity or where no valid data is expected due to low laser intensity. Images were analyzed with a multi-pass, cross-correlation method with a 32×32 pixel interrogation window and 75% overlap. Vector post-processing was done using two passes of a universal outlier detection (UOD) filter with an 11×11 filter window region and a threshold of r > 1.5 [23]. These

post-processed vector fields were then imported into Matlab to perform statistical analysis.

2.3.3 Statistics

All the post-processed vector fields were used in Matlab for statistical plots. The tunnel coordinates are defined as X, Y and Z.

For the side-on PIV orientation, all the data was acquired at 12°chordwise coordinates defined as x_c and y_c. As this orientation has two FoVs, the origin for the first FoV is set to be at the leading edge and the second FoV moved 24mm upstream and 5mm in the negative y-axis from the first FoV (Fig2.9). The streamwise and wall-normal, mean and fluctuating velocities in these coordinates are defined as U_c, u' and V_c, v', respectively. The x_c and y_c coordinates were non-dimensionalized by the chord length at the PIV data acquisition region which is 193 mm (7.6 inches).

For the mean streamwise (U_c) and wall-normal (V_c) velocities, all the vectors were time-averaged in 3rd dimension (time), which is the number of frames for each data set. Fluctuating velocities are extracted by subtracting the mean velocity from the instantaneous velocities.

$$u_c = U_c + u' \tag{2.1}$$

$$v_c = V_c + v' \tag{2.2}$$

Using these mean and fluctuating velocities in streamwise and wall-normal directions, Reynolds shear stress is plotted as $(-\overline{u'v'})$, Reynolds streamwise normal stress as $(\overline{u'}^2)$, Reynolds wall-normal normal stress as $(\overline{v'}^2)$ and In-plane turbulent kinetic energy as $(\overline{u'}^2 + \overline{v'}^2)/2$.

For the top-down configuration, all the data was acquired tangent to the wing but parallel to the chord. The origin is set to be the lower left corner of the FoV with incoming flow. The coordinates for this configuration are defined as x_t and z_t. The leading edge is approximately at $x_t/c = 0.35$ and sweeps towards the tip with 35° angle. The streamwise and spanwise, mean and fluctuating velocities are defined as U_t, u'_t and W_t, w'_t respectively.

$$u_t = U_t + u'_t \tag{2.3}$$

$$w_t = W_t + w'_t \tag{2.4}$$

These velocities were non-dimensionalized using the x-component of the free stream velocity U_∞ and wing sweep angle (θ) as $U_\infty \cos\alpha * sin\theta$. The wing sweep angle is 35°.

Chapter 3

RESULTS

Flow visualization was used to determine the test conditions for PIV experiments. A nominal case was set at Reynolds number and angle of attack of Re = 10^6 and AOA = 12°. To explore the sensitivity of this nominal condition, PIV measurements were also obtained at two adjacent angles of attack 10.5 and 13.5 degrees as well as two additional Reynolds numbers 5×10^5 and 1.48×10^6.

The location for the PIV experiment was determined to be about 432 mm (17 inches) from the tip of the wing as shown in Fig: 2.5. For simplicity, we defined Reynolds numbers 5×10^5, 10^6 and 1.48×10^6 as Re 1, Re 2 and Re 3, respectively. A summary of PIV testing conditions for both orientations is presented in Table: 3.1.

The results for the second field of side-on PIV of view are not presented in the following sections because all the statistical plots look similar to the first field of view at different Reynolds numbers and angles of attack (AOA).

3.1 Nominal case

In this section, the flow behaviour of the nominal conditions in both orientations is explored. Fig 3.1 and Fig 3.2 depicts the mean velocities and Reynolds stress variation for the nominal case. It is seen that the flow separates near the leading edge with some reverse flow in the

Reynolds Number	**Side-on PIV FoV 1 & 2 AOA**	**Top-down PIV AOA**
Re 1 (5×10^5)	12°	12°
Re 2 (10^6)	10.5°, 12°, 13.5°	12°
Re 3 (1.48×10^6)	12°	

Table 3.1: PIV Testing conditions for both orientations

separated region above the wing surface. The wall-normal velocity is maximum near the leading edge as the flow accelerates.

The turbulent shear stress from Fig 3.1(c), is greatest along the separated shear layer and negative, indicating turbulent production. In Fig 3.1(d), the in-plane TKE is highest near the hypothesized point of separation and spreads out and becomes weaker as it convects downstream. The streamwise Reynolds normal stress (u') is also higher near the separation point as shown in Fig 3.2(a) and decreases downstream further from the separation point while the wall-normal fluctuating velocity (v') is higher in the downstream flow away from the separation point as seen in Fig 3.2(b).

In the top-down orientation, the flow moves from the left to the right. Since the wing has a sweep angle, the flow has spanwise velocity from root to tip (bottom to top) as shown in Fig (3.3). The mean streamwise velocity is negative in the separated region with the reverse flow indicated by streamlines in Fig 3.3. In Fig 3.6, we can see turbulence is produced near the leading edge during separation. The fluctuating velocities are also higher near the leading edge as seen in Figures 3.7 and 3.8.

A small dark region in the middle of the spanwise direction from figures 3.5 to 3.7 is due to bad data. This bad data is thought to be some false vectors from background images leading to nonuniform turbulence. The spanwise fluctuations are positive as the flow moves from root to tip in a positive z_c axis as shown in Fig 3.8. The region with maximum spanwise fluctuations near the plot's rightmost corner is considered non-physical.

From mean statistics plots in fig 3.1, we can see flow accelerates due to the shape and curvature of the wing. As the air flows the upper surface of the wing has higher velocity than the lower surface creating a difference in pressure for lift. These plots also indicate flow separates near the leading edge with no reattachment in the streamwise direction. The wall-normal velocity in the separated region seems to have a small fraction of reversed flow downstream of the FoV. From Fig 3.3, it is clear that the separated flow near the leading edge results in reverse flow in the streamwise direction. This region of separated flow is also seen in side-on orientation. The result from tufts flow visualization in fig 2.5 is also separated in this region on the wing surface. The flow is mostly moving spanwise because of the sweep angle with no reverse flow in this direction. Reynolds shear stress, in-plane TKE

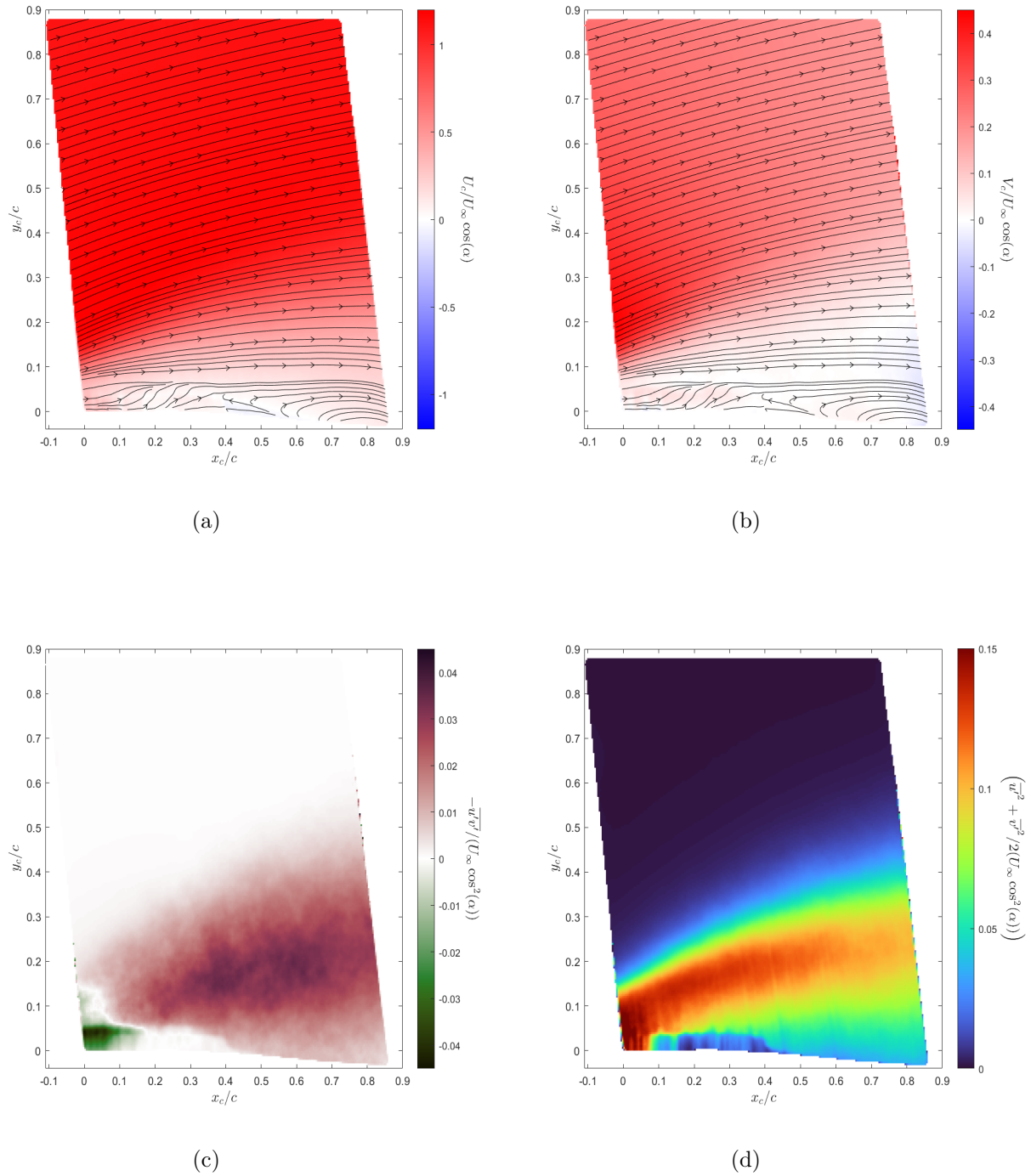

Figure 3.1: Side-on PIV nominal case, (a) Mean streamwise, (b) Mean wall normal, (c) Reynolds shear stress, and (d) In-plane TKE

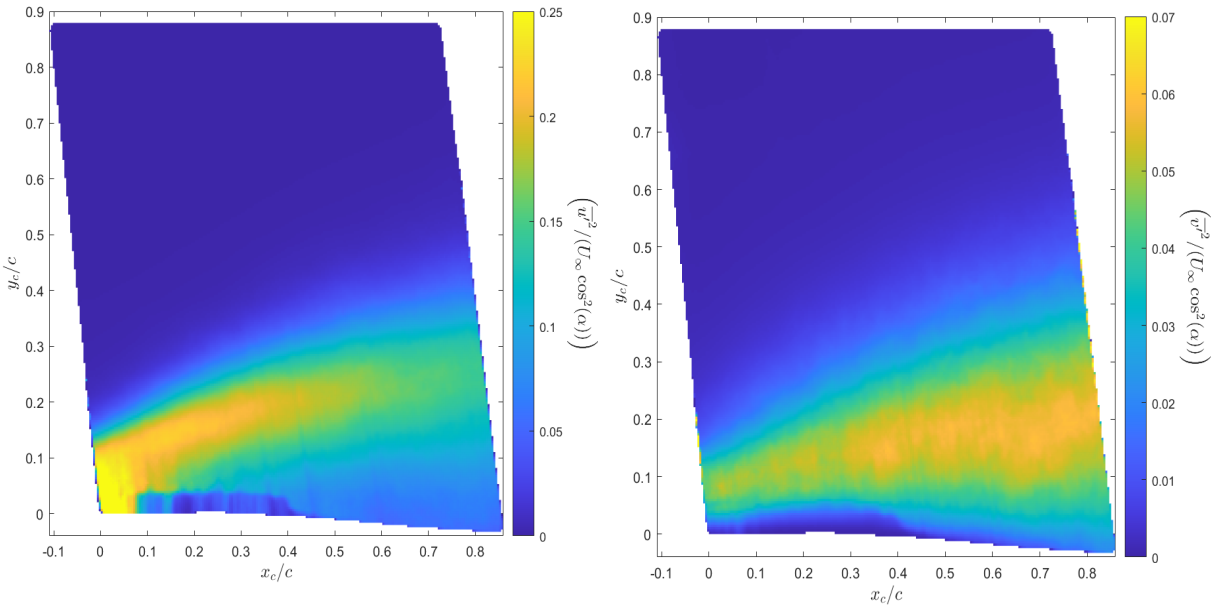

(a) (b)

Figure 3.2: Nominal case Reynolds Normal stresses, (a) streamwise (u'), and (b) wall-normal (v')

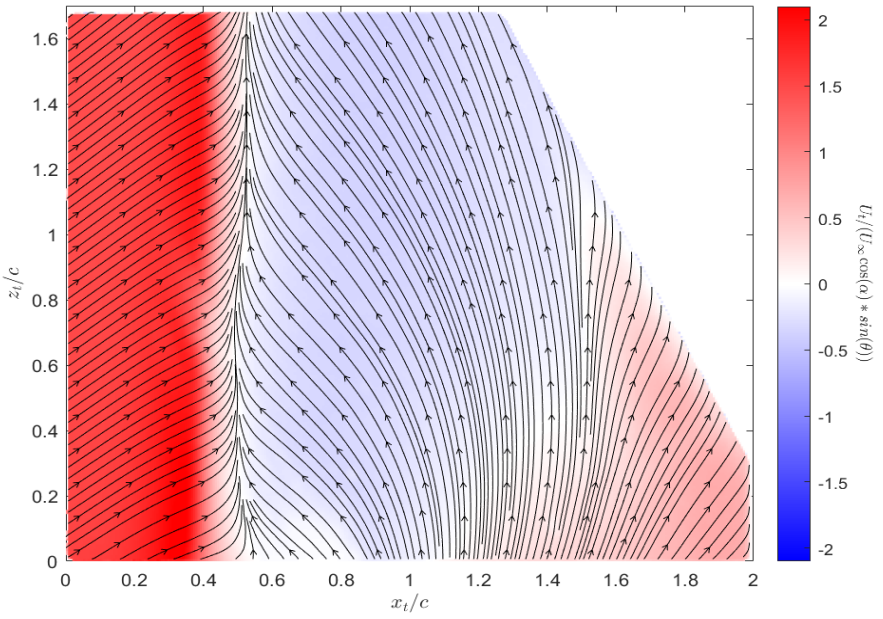

Figure 3.3: Top-down PIV nominal case Mean streamwise velocity

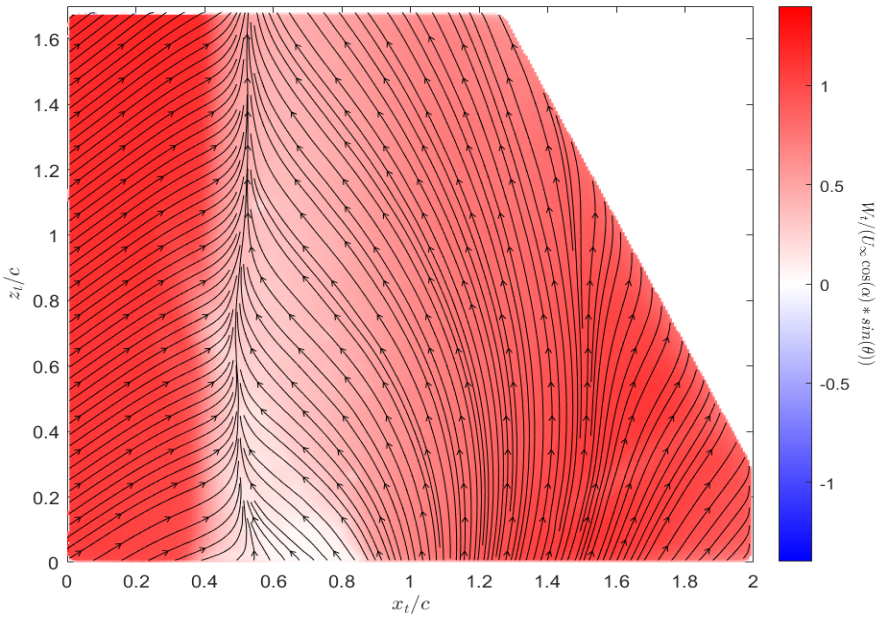

Figure 3.4: Top-down PIV nominal case Mean spanwise velocity

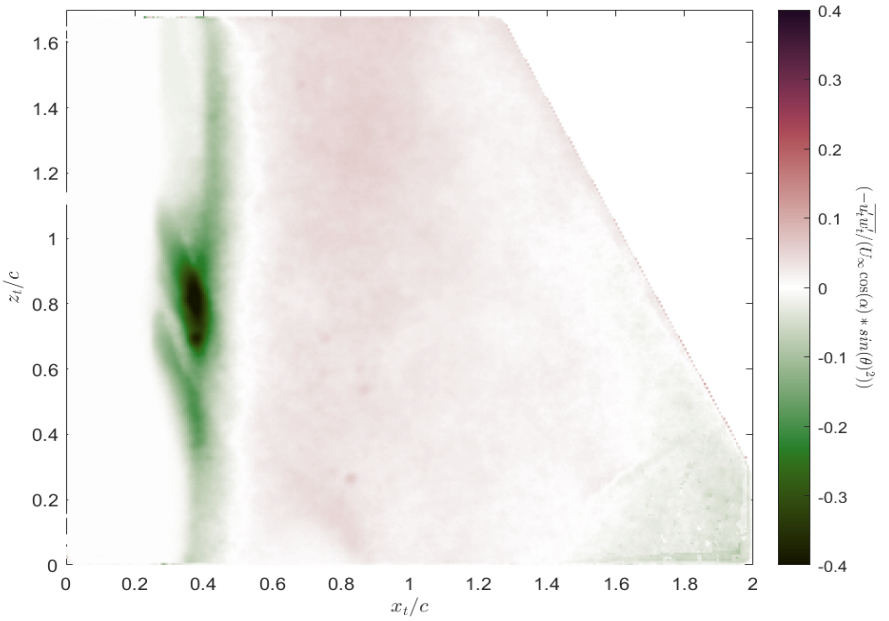

Figure 3.5: Top-down PIV nominal case Reynolds shear stress

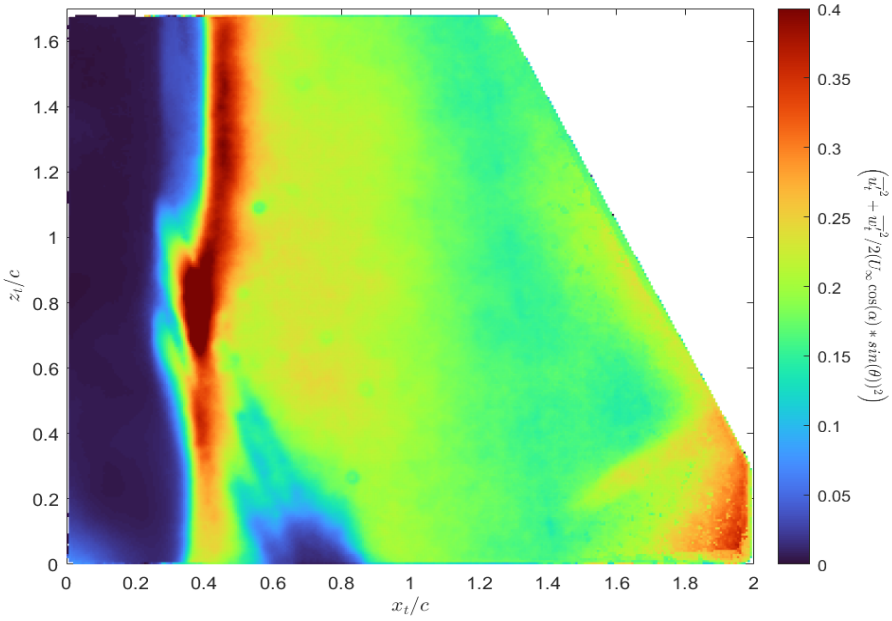

Figure 3.6: Top-down PIV nominal case In-plane TKE

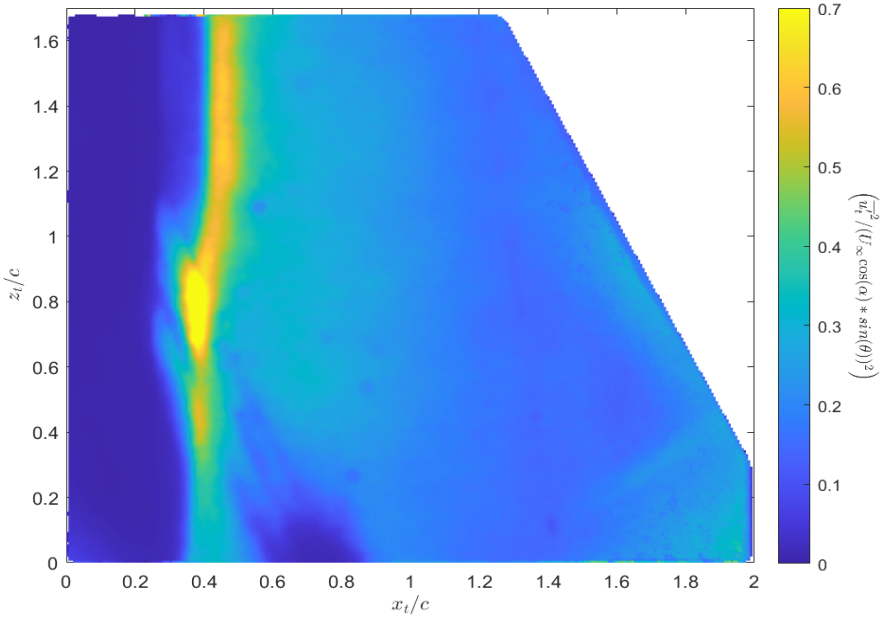

Figure 3.7: Top-down PIV nominal case streamwise Reynolds normal stress

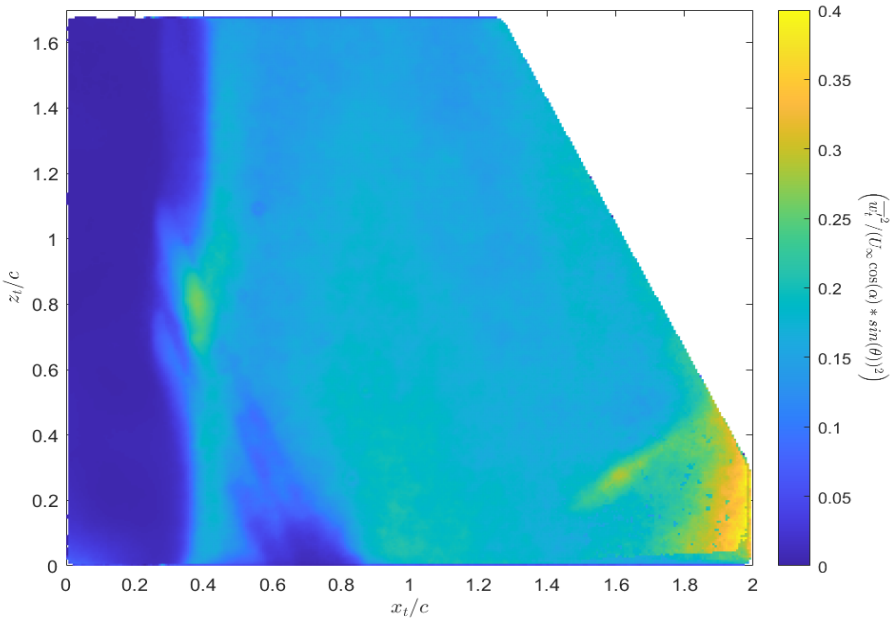

Figure 3.8: Top-down PIV nominal case spanwise Reynolds normal stress

production is seen near the leading edge from both of these orientations. The in-plane TKE is maximum near the leading edge separation and becomes weaker as it convects downstream in both orientations.

3.2 Influence of angle of attack

We now explore the sensitivity of the flow to changes in the angle of attack at Re 2. We can see flow separation increases with increasing AOA as shown in Fig: 3.9. The mean streamwise velocity is always higher closer to the leading edge due to the geometry of the wing surface. The mean wall-normal velocity suggests high reverse and vertical flow with increasing AOA with maximum wall-normal velocity near the leading edge as shown in Fig: 3.10.

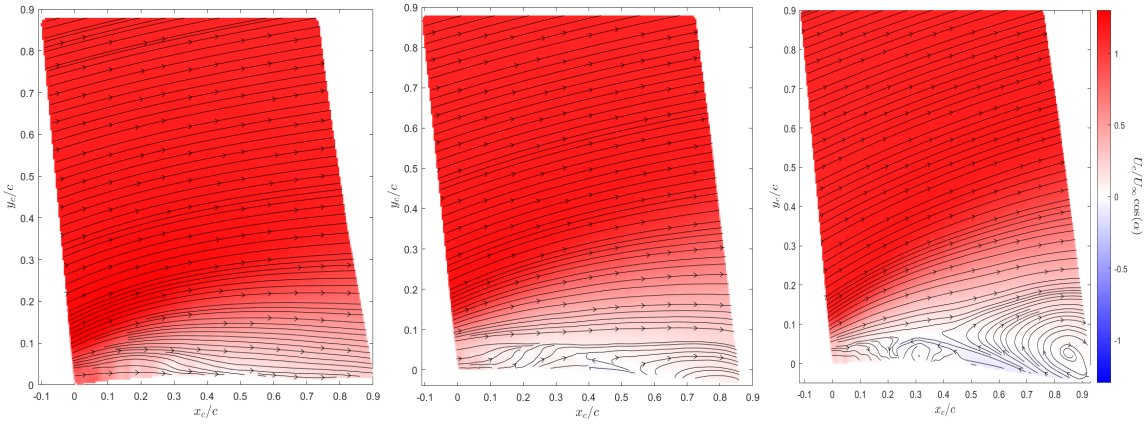

Figure 3.9: Mean streamwise velocities at AOA. (a) 10.5, (b) 12 and (c) 13.5

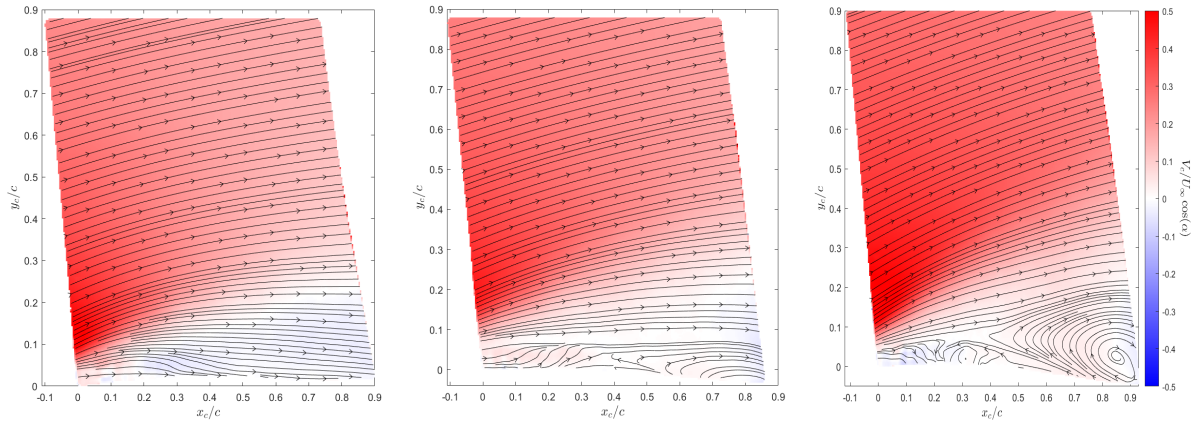

Figure 3.10: Mean wall-normal velocities at AOA. (a) 10.5, (b) 12 and (c) 13.5

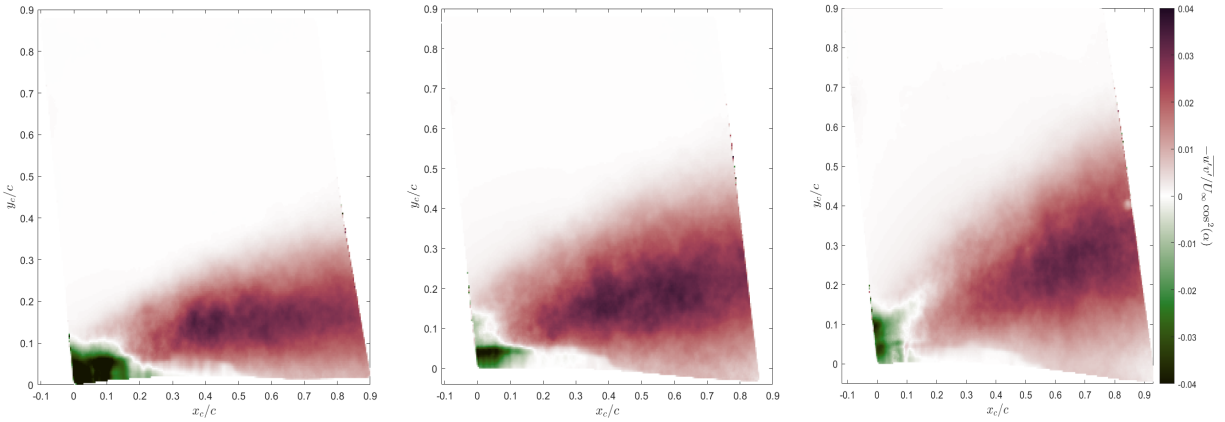

Figure 3.11: Reynolds Shear stresses at AOA. (a) 10.5, (b) 12 and (c) 13.5

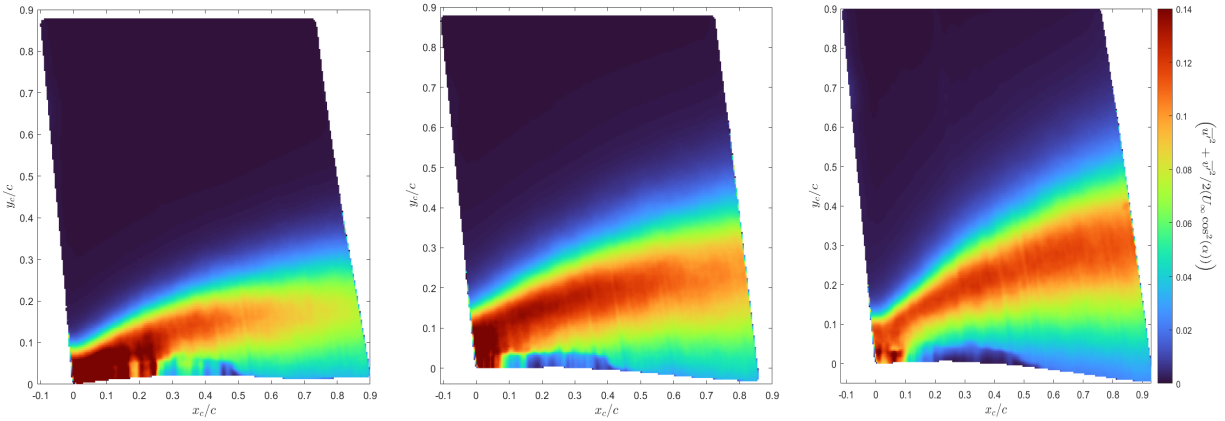

Figure 3.12: In-plane Turbulent Kinetic Energy at AOA. (a) 10.5, (b) 12 and (c) 13.5

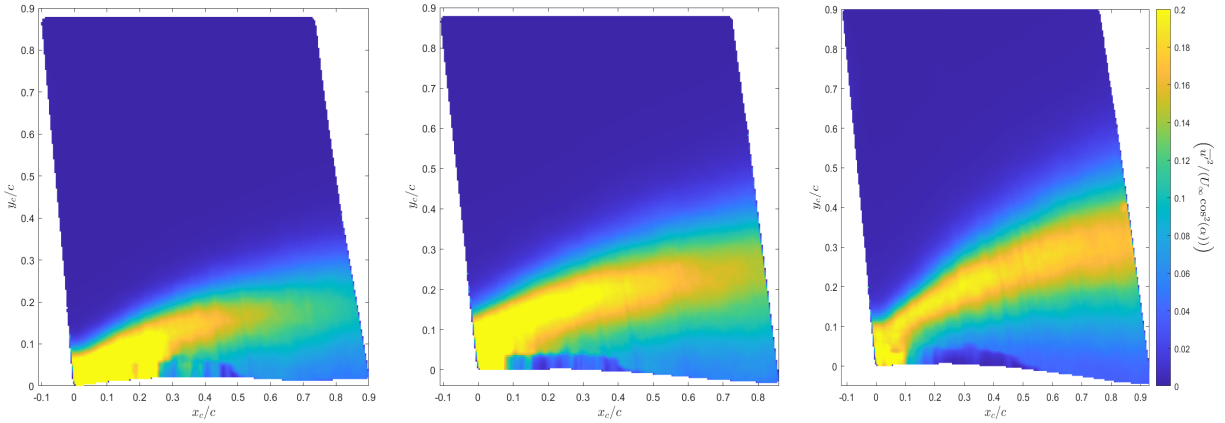

Figure 3.13: Reynolds Normal stress (u') at AOA. (a) 10.5, (b) 12 and (c) 13.5

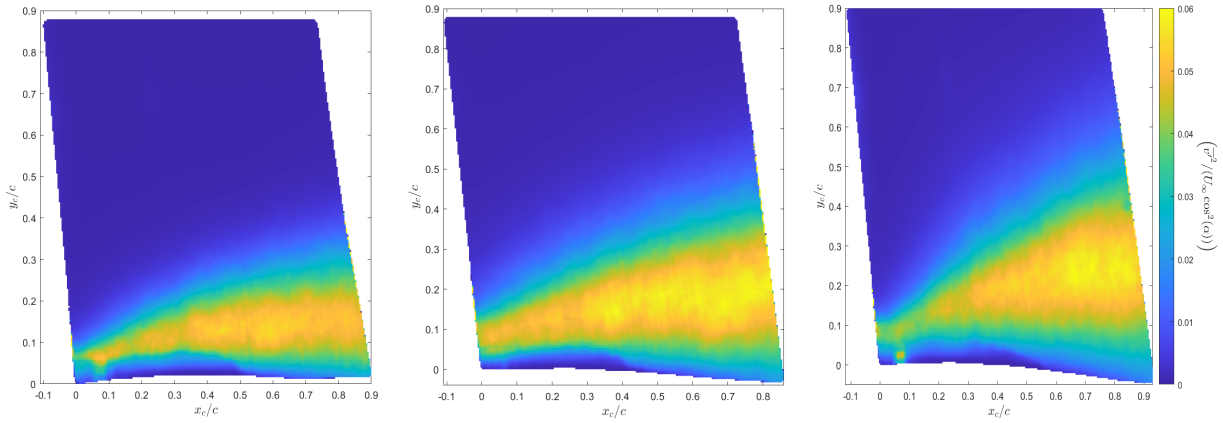

Figure 3.14: Reynolds Normal stress (v') at AOA. (a) 10.5, (b) 12 and (c) 13.5

The difference in boundary layer thickness (y_c/c) also varies from 0.3 to 0.4 approximately. In Fig: 3.11, the maximum shear stress occurs further downstream with increasing AOA and the angle of the shear layer is more than the difference in AOA indicating a difference in separation bubble. The region of turbulent kinetic energy extends further downstream with increasing AOA and the shear layer gets wider with less turbulent intensity than lower AOA cases as presented in Fig: 3.12, this suggests a wider shear layer with less turbulent intensity than lower AOA cases. The region of streamwise fluctuating normal stress (u') extends further downstream with increasing AOA as seen in Fig: 3.13. The width of the shear layer gets wider but, the peak normal stresses are lower. The wall-normal fluctuating velocity (v') is also increasing with AOA presented in Fig: 3.14, with similar magnitudes at AOA 12°, 13.5°and least at 10.5°. The dark red and bright yellow region near the leading edge in Fig: 3.12 and 3.13, is thought to be non-physical and the result of imperfect masking of the near-wall and upstream portions of the image.

3.3 Influence of Reynolds number

We now explore the sensitivity of the flow separation to the Reynolds number. By comparing the flow statistics at Re 1, 2 and 3 at AOA 12°(see Fig 3.15), the boundary layer thickness is decreasing with increasing Reynolds number as expected. We also see flow acceleration near the leading edge due to the wing geometry. The mean wall-normal velocity suggests similar reverse and vertical flow across different Reynolds numbers but with small differences in the

separated region as shown in Fig: 3.16.

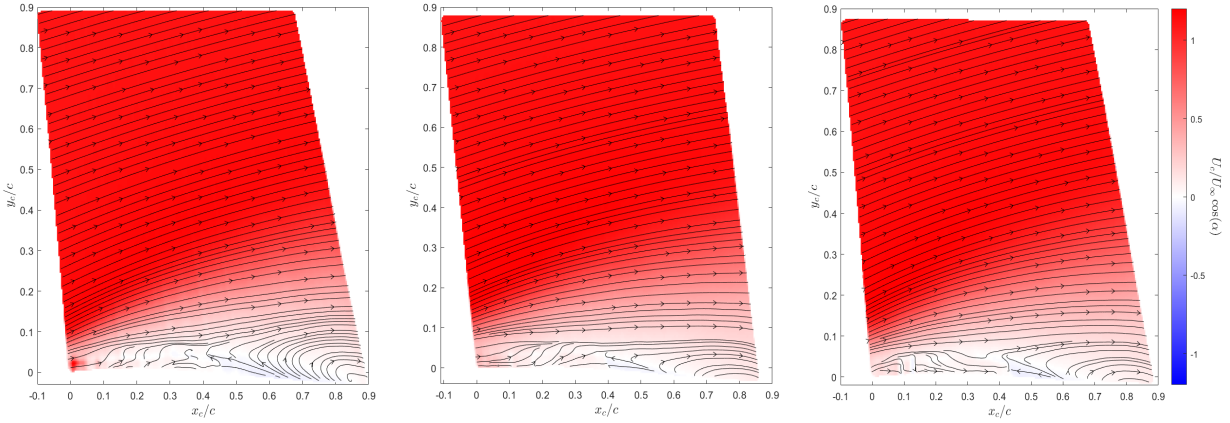

Figure 3.15: Mean streamwise velocities at (a) Re 1, (b) Re 2 and (c) Re 3

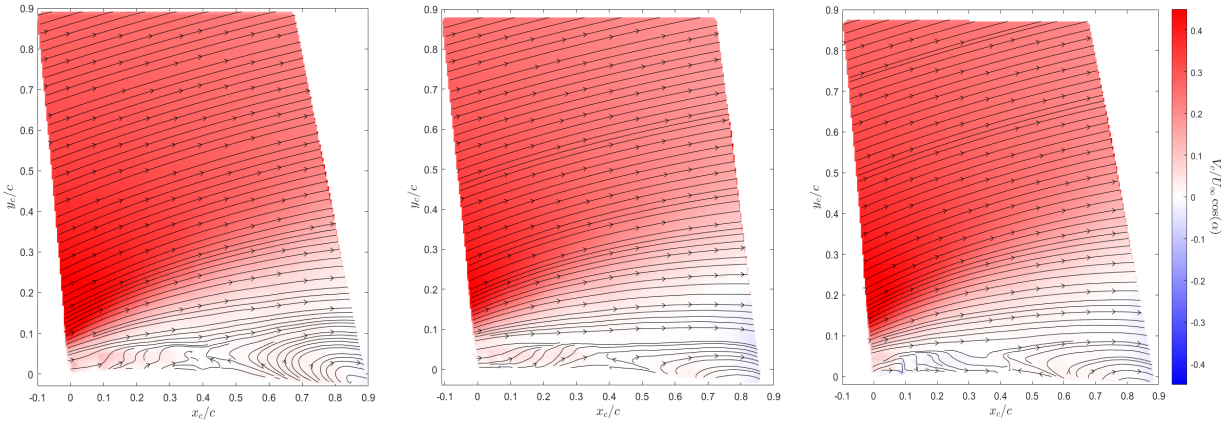

Figure 3.16: Mean Wall-normal velocities at (a) Re 1, (b) Re 2 and (c) Re 3

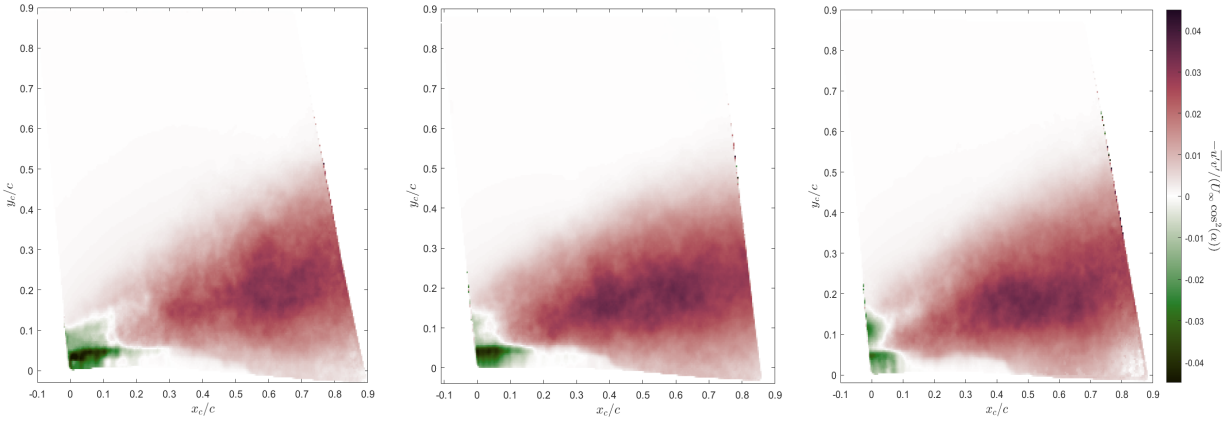

Figure 3.17: Reynolds shear stresses at (a) Re 1, (b) Re 2 and (c) Re 3

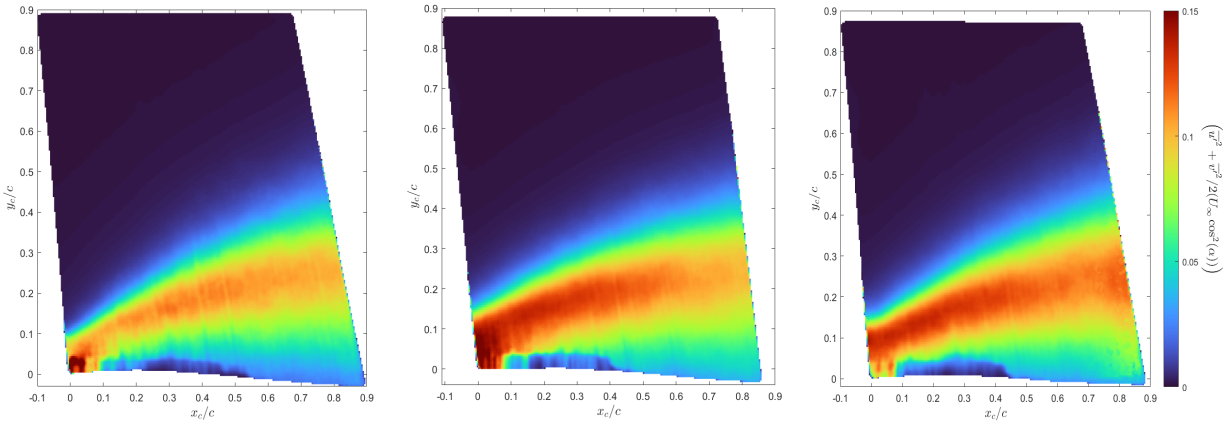

Figure 3.18: In-plane Turbulent Kinetic Energy at (a) Re 1, (b) Re 2 and (c) Re 3

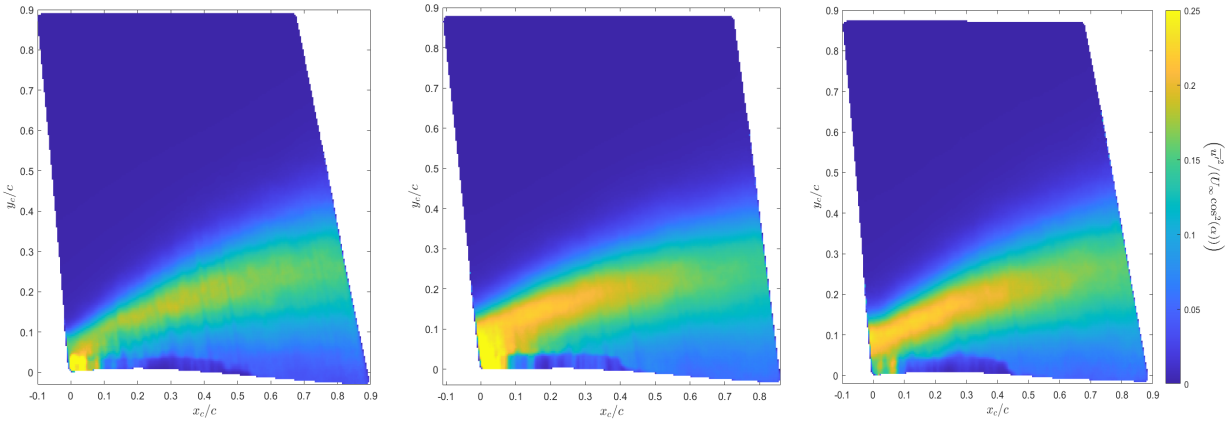

Figure 3.19: Reynolds Normal stress (u') at (a) Re 1, (b) Re 2 and (c) Re 3

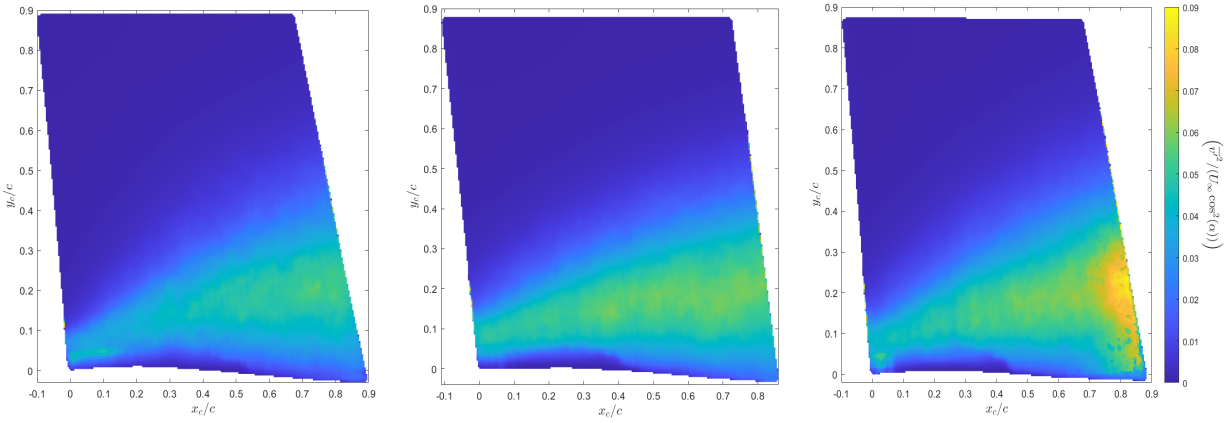

Figure 3.20: Reynolds Normal stress (v') at (a) Re 1, (b) Re 2 and (c) Re 3

In the separated region we can see more positive velocities at low Re (Re1) and a few at high Re (Re 3). The Reynolds shear stresses in the separated region are similar at Re 2 and Re 3 and reduced at Re 1 as shown in Fig: 3.17, due to a lower Reynolds number. The in-plane TKE has a local maximum along the shear layer as shown in Fig: 3.18. The In-plane TKE and fluctuating streamwise normal stress (u') are very similar at Re 2 and Re 3 and lower at Re 1. The wall-normal fluctuating velocity (v') increases with the Reynolds number as shown in Fig: 3.20. The maximum wall-normal stresses are in the downstream part of the separated region at Re 3.

From Fig 3.21, the flow in the separated region has more reverse flow at Re 1 than Re 2. This decrease in flow separation with increasing Re was also noted from side-on PIV. The mean separation point is approximately near $x_t/c = 0.45$ and this is not an exact value as the data was acquired above the surface. This separation is not defined by $C_f = 0$, as the flow is three-dimensional. The flow on the wing surface is spanwise from root to tip (bottom to top) and the flow downstream gains velocity after the separated region near the trailing edge. The mean spanwise velocity is positive as flow is mostly going towards the tip in a positive z_c direction and is very similar at both Reynolds numbers. From fig: 3.22, near the trailing edge at approximately $x_c/c = 1.65$ the flow is more attached at Re 2 than Re 1. The turbulent energy is produced at the leading edge, as shown in Fig 3.24 and this energy dissipates going downstream. The Turbulent shear stress and streamwise normal stresses are similarly higher at the leading edge and dissipate downstream as seen in figures 3.23 and 3.25. The spanwise normal stresses have similar magnitudes at both Reynolds numbers as seen in Fig 3.26.

For the case at Re 1, the data set has some bad vectors at the downstream part of the FoV. For the case at Re 2, some bad vectors are at a point in the middle of the leading edge. As these are nonuniform and non-physical they are thought to be false vectors from background images.

3.4 Regions of Bad vectors

As seen in the results we saw a few bad vectors in both orientations with dark regions. These dark regions are due to false vectors from background images leading to non-uniform

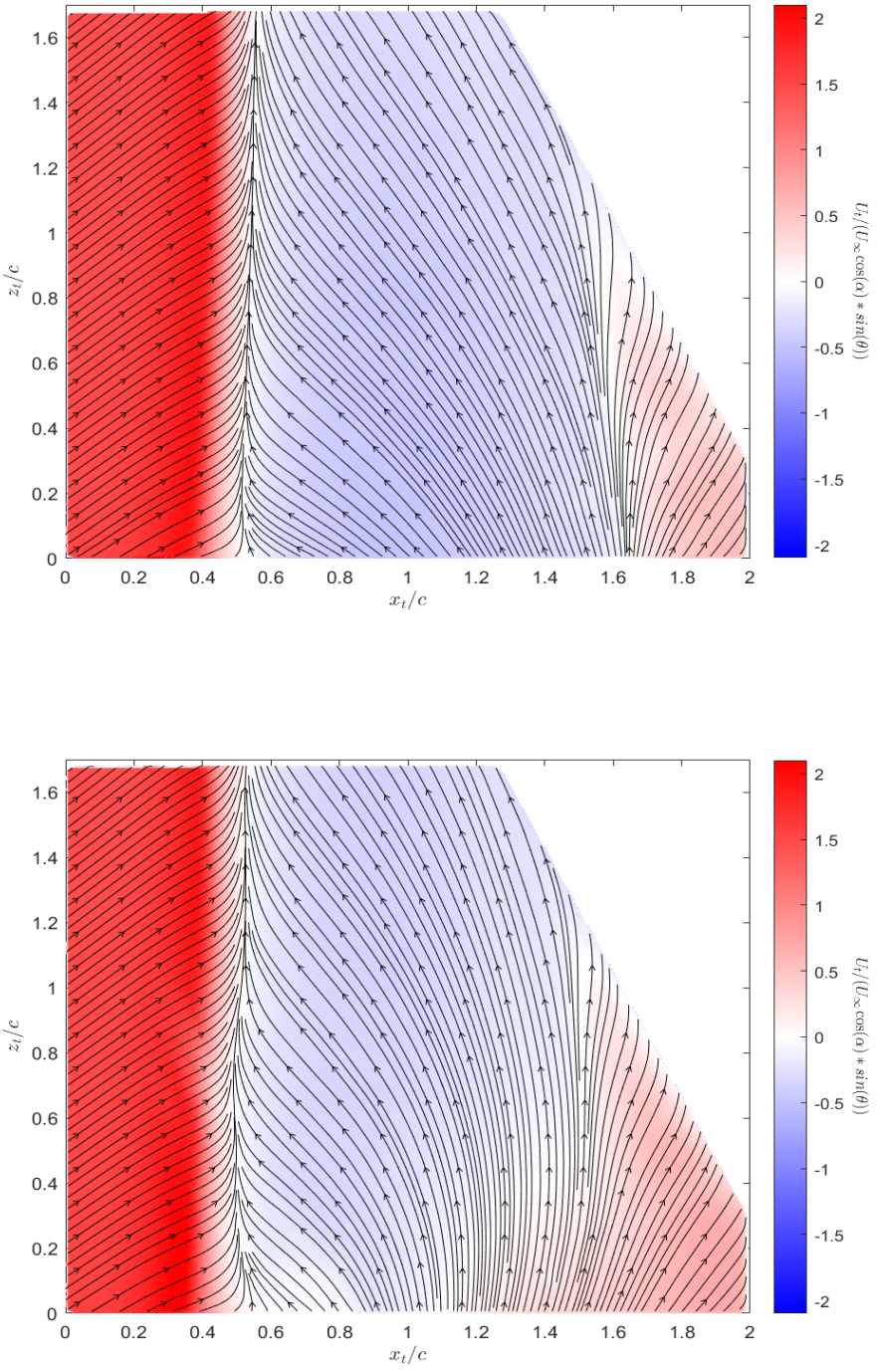

Figure 3.21: Mean streamwise velocity at (a) Re 1 and (b) Re 2

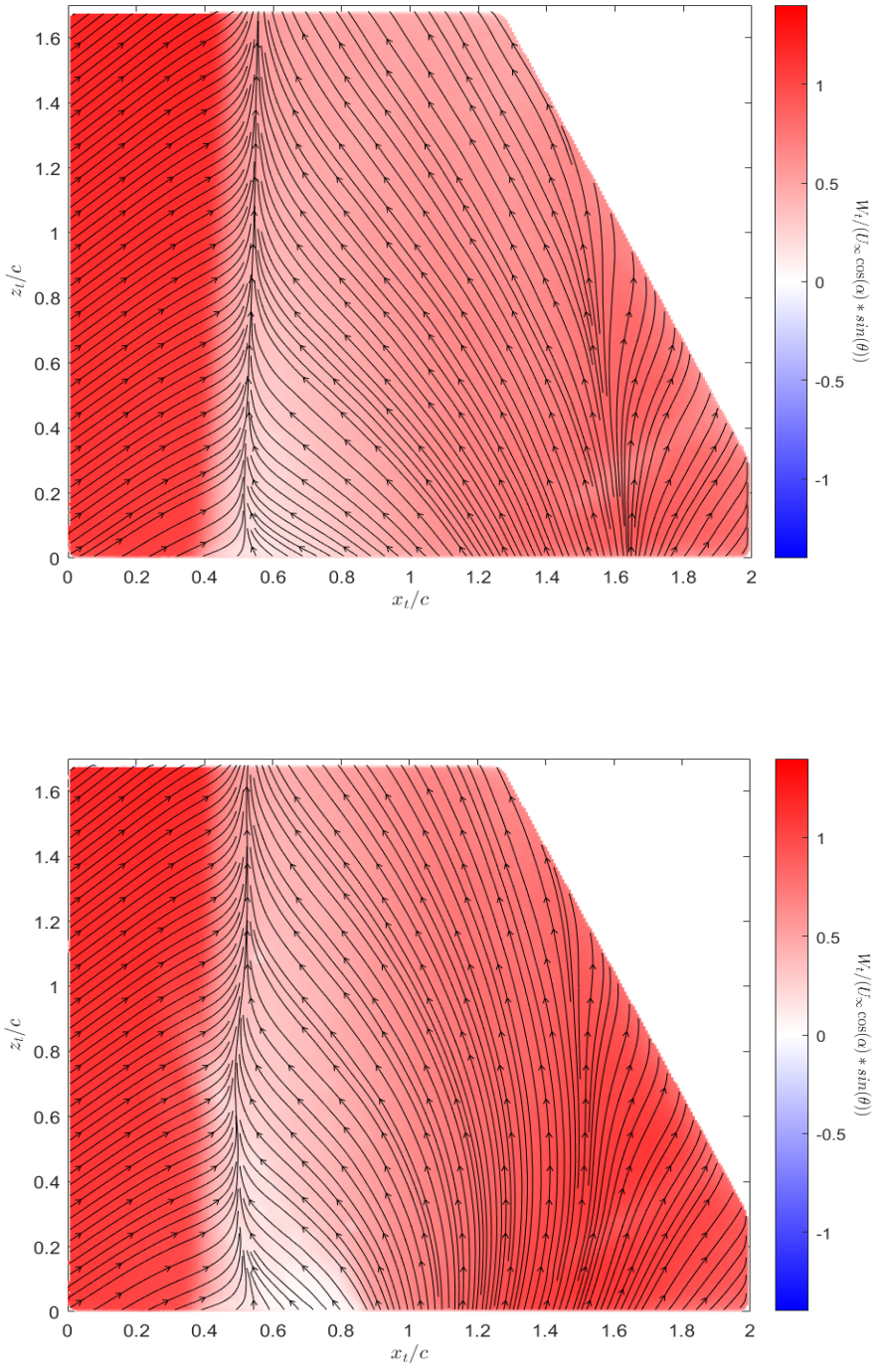

Figure 3.22: Mean spanwise velocity at (a) Re 1 and (b) Re 2

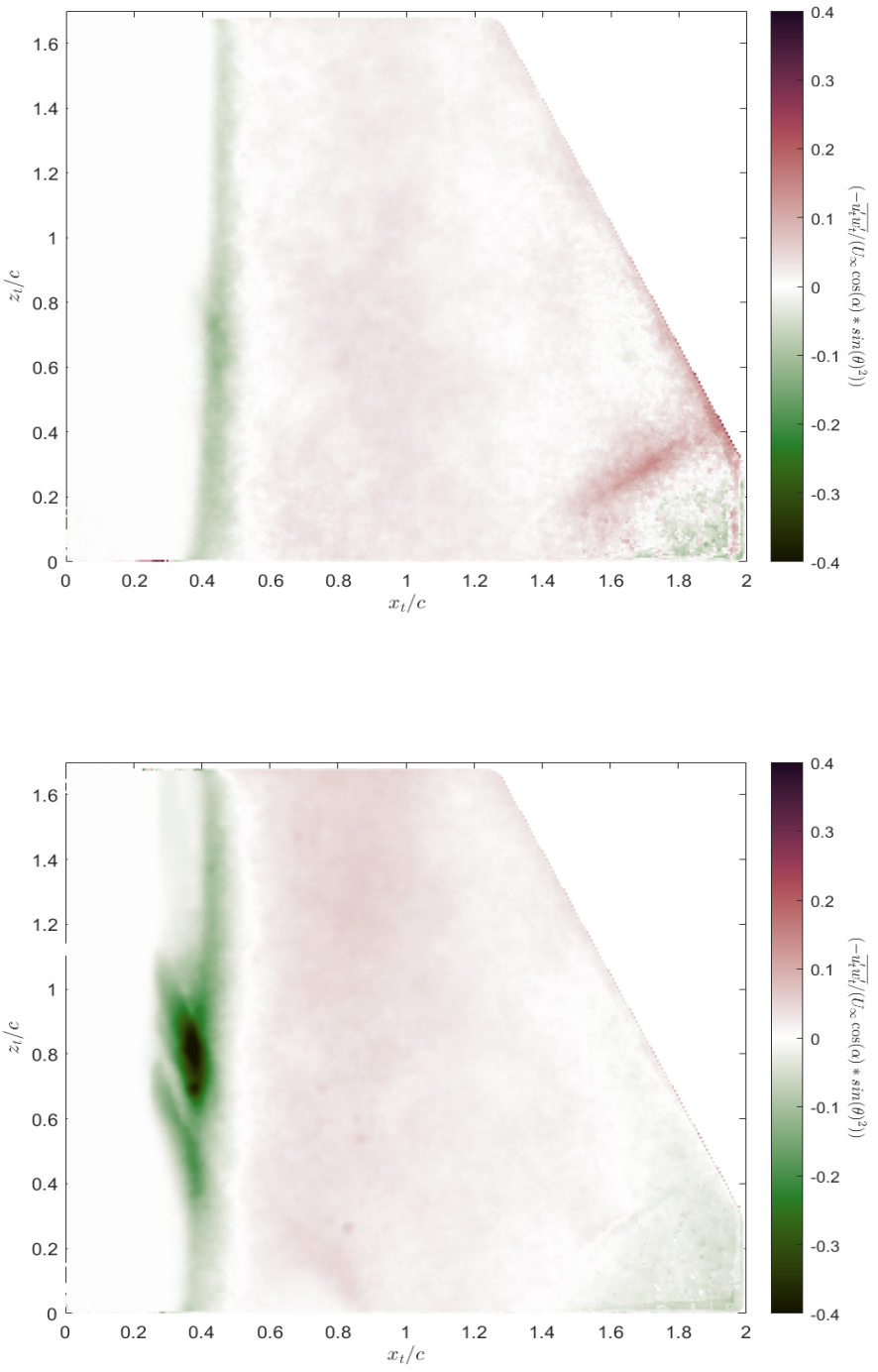

Figure 3.23: Reynolds shear stress at (a) Re 1 and (b) Re 2

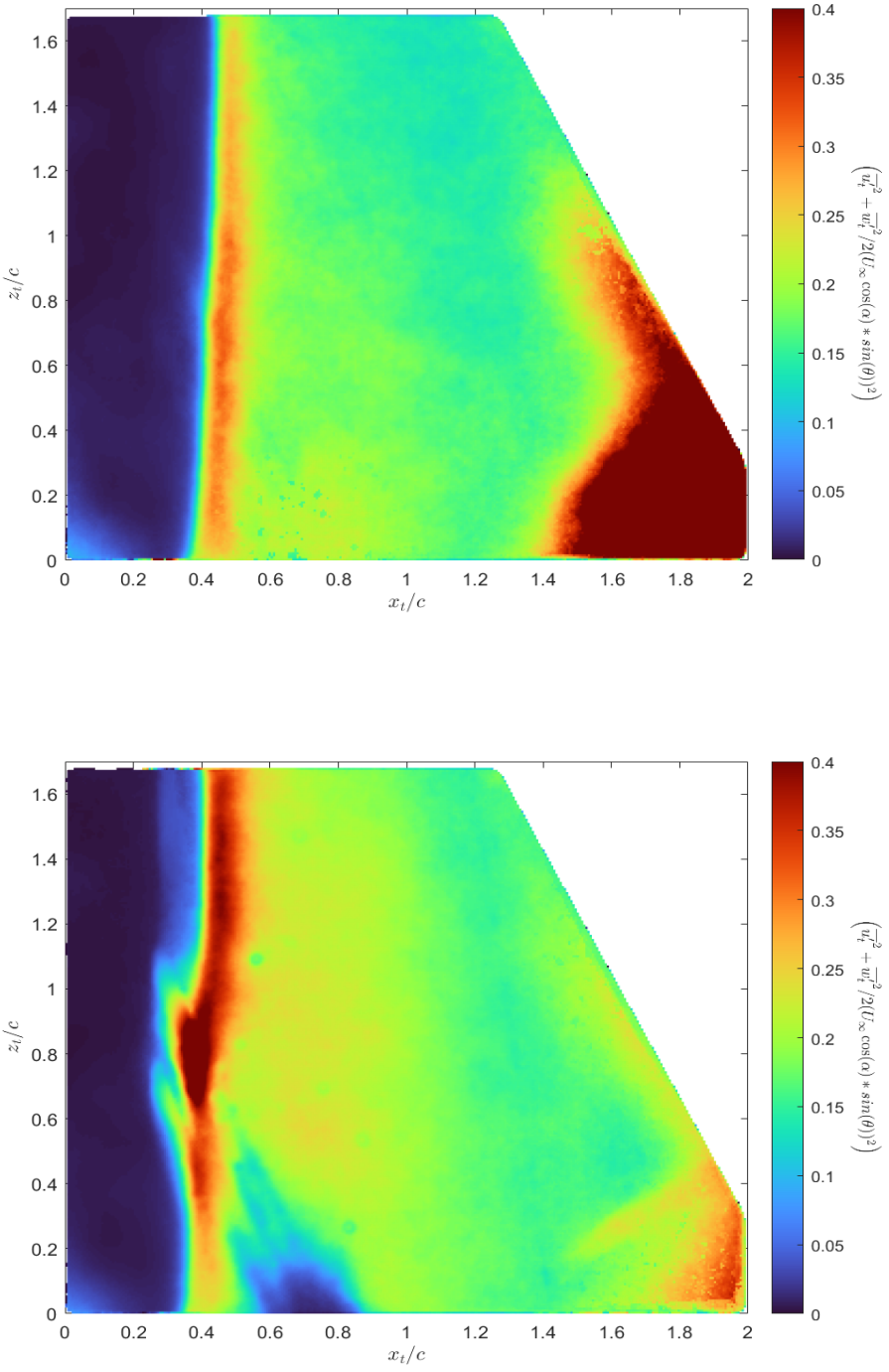

Figure 3.24: In-plane TKE at (a) Re 1 and (b) Re 2

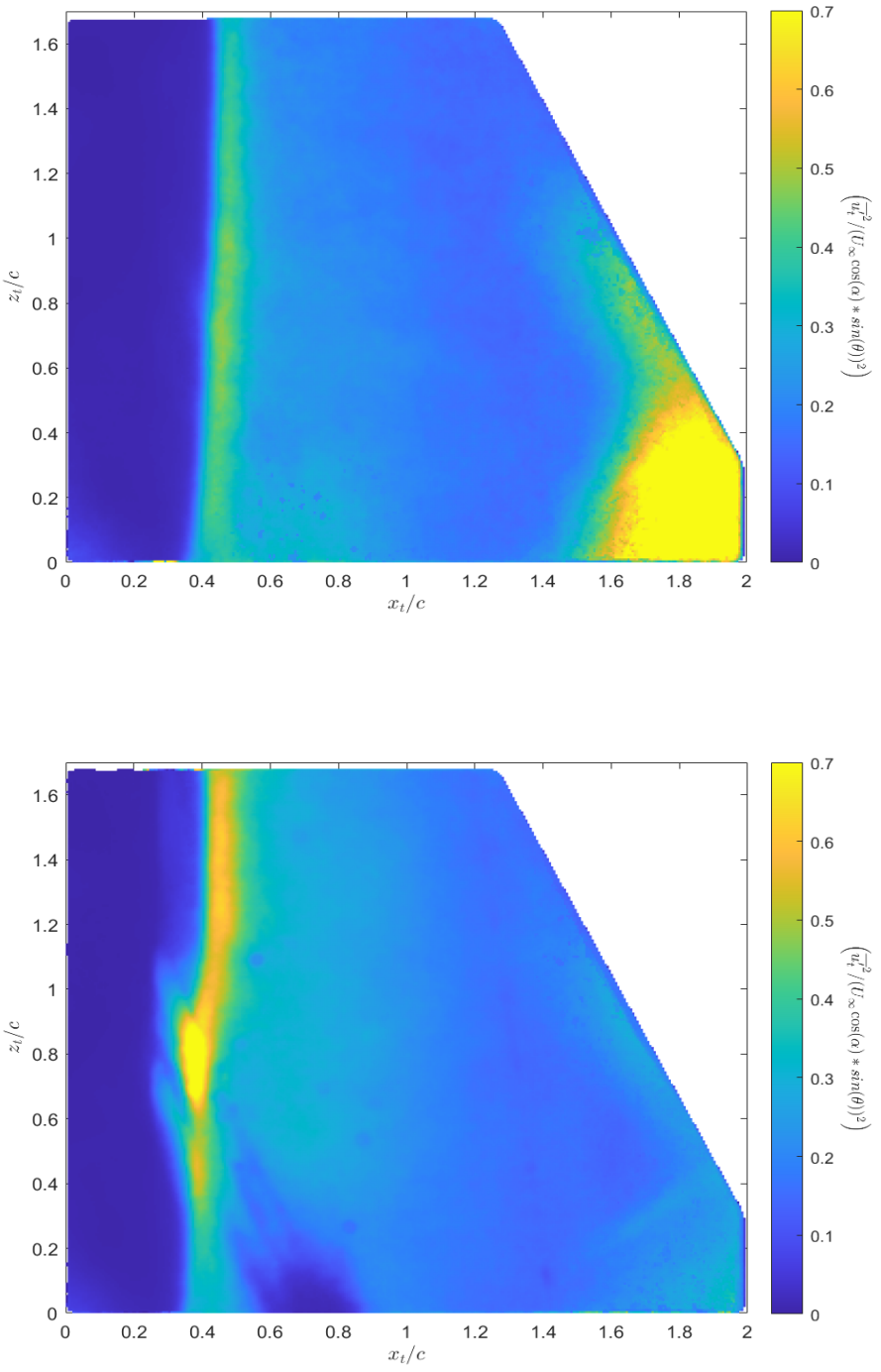

Figure 3.25: Reynolds streamwise normal stress (u') at (a) Re 1 and (b) Re 2

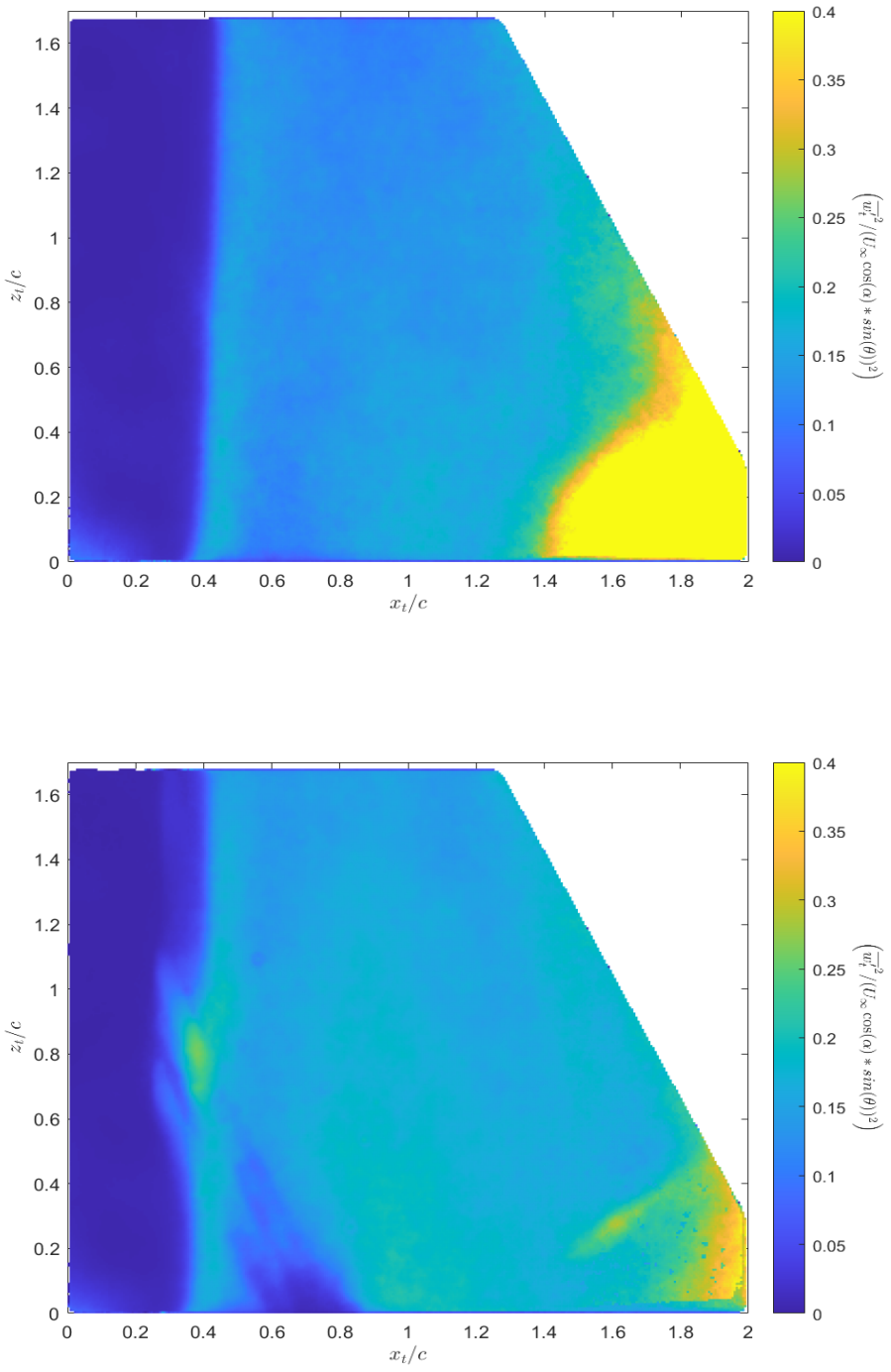

Figure 3.26: Reynolds spanwise normal stress (w') at (a) Re 1 and (b) Re 2

turbulence. From Fig: 3.27, we see a region of high laser reflection on the wing surface marked in red colour, these regions are brightly illuminated and lead to bad vectors as the PIV can not keep track of particles.

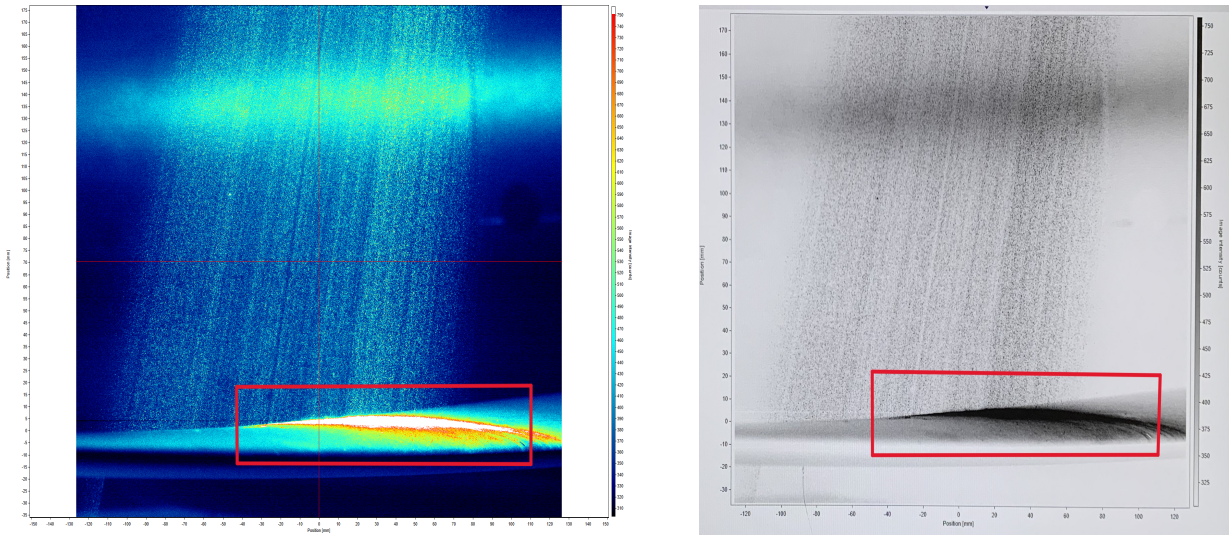

Figure 3.27: PIV Raw image (left) and PIV background subtracted image (right) with regions of bad vectors from side-on PIV

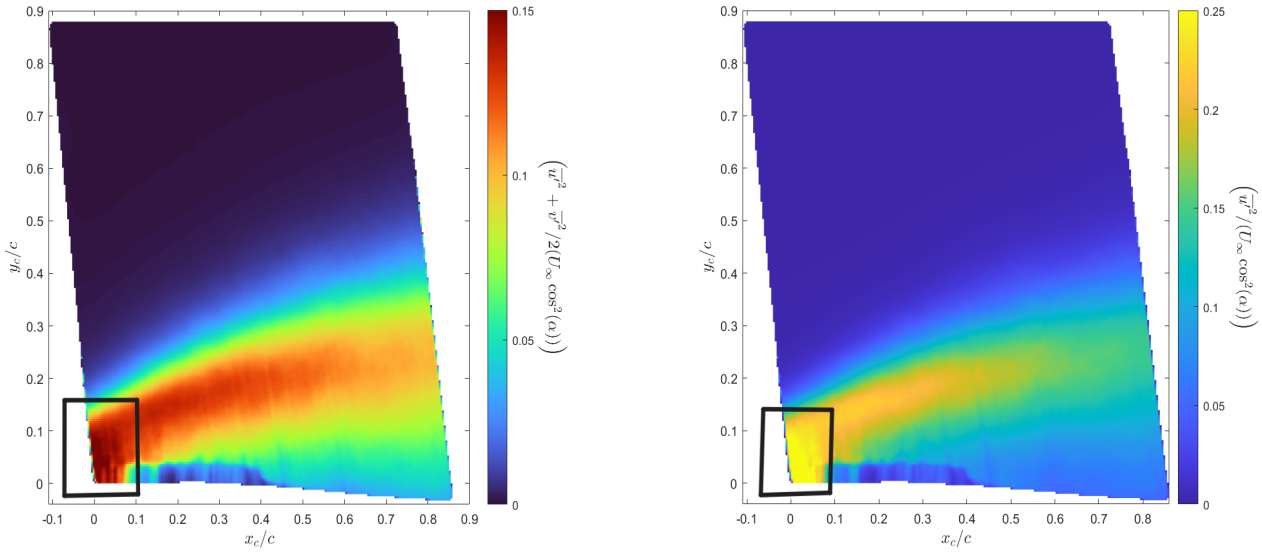

Figure 3.28: Regions of bad vectors in side-view processed images

Similarly, for the top-down orientation, we have bad vectors near the leading edge and trailing edge as shown in Fig: 3.29. The highly reflected region near the leading edge is due to the higher density of seeding particles being stuck from the flow during long runs. The bad vectors near the trailing edge are due to high reflections from the test section floor.

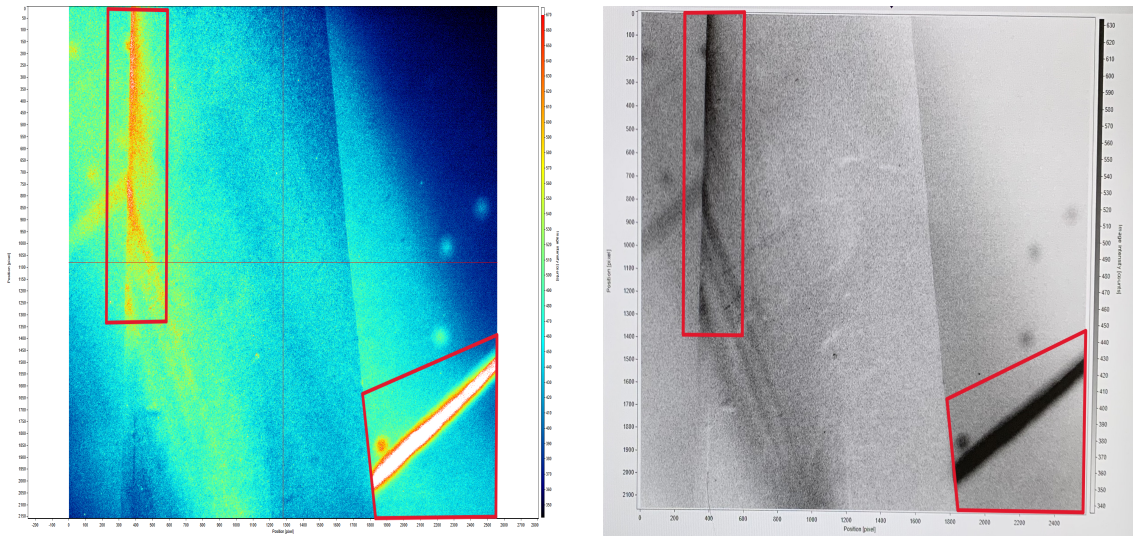

Figure 3.29: PIV Raw image (left) and PIV background subtracted image (right) with regions of bad vectors from top-down PIV

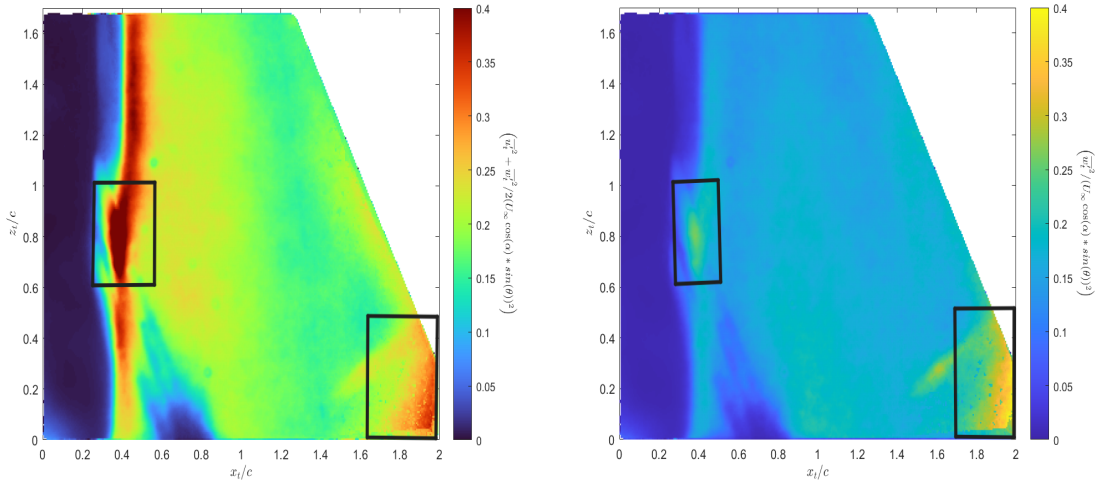

Figure 3.30: Regions of bad vectors in top-down processed images

In these regions, as the particles are very bright, it is hard to keep track of particles between two frames, leading to false vectors. To better improve the data collected from PIV and to increase the signal-to-noise ratio we can reduce the effect of reflection from surfaces and clean the regions of possible accumulation of high-density particles. Doing this might give us good vectors in the flow field and hence good data for turbulence analysis.

Chapter 4

CONCLUSION

This study aims to explore turbulence separation on a 4% half-body High-Speed Common Research Model (CRM-HS). To explore the turbulence, a non-intrusive PIV experimentation is used to capture the flow fields for statistical analysis. To study the dynamics of flow separation in streamwise and spanwise directions a PIV experiment was performed in side-on and top-down orientations. Side-on PIV highlights the separated shear layer and top-down PIV gives spanwise flow dynamics. Using tufts flow visualisation the test conditions for the PIV experiment are determined with a nominal case at Re = 10^6 and AOA 12°. To explore the sensitivity of the separation, data was acquired 1.5° on either side of AOA 12° and at Reynolds numbers of 5×10^5 and 1.48×10^6. The test location was determined to be about 432 mm (17 inches) from the wing tip, where the chord length is 193 mm (7.6 inches). This experiment is also a first step in applying the PIV experiment method in a big-scale facility like Kirsten Wind Tunnel at the University of Washington, Seattle. This experiment on the CRM-HS stall will be used as a testbed for understanding the dynamics of a more complex CRM-HL model in future. It plays a key role in many upcoming tests on CRM-HL wing geometry to acquire high-quality experimental data for CFD validation studies.

In the nominal case, the side-on PIV turbulence exploration implies flow separation with a small boundary layer and wall-normal velocity peaks near the leading edge due to flow acceleration. The in-plane TKE and streamwise (u') normal stress is highest near a hypothesized point of separation near the leading edge and becomes weaker as it convects downstream. The turbulent shear stress is greatest along the separated shear layer indicating turbulence production, while wall-normal v' normal stress is higher in the flow downstream away from the separation point. In top-down PIV, the flow is reversed near the wing surface in the streamwise direction and moves from root to tip in the spanwise direction. Turbulence is

produced near the leading edge during separation and fluctuating velocities are also higher near the leading edge.

As AOA increases at Re = 10^6, the flow separation and reverse flow also increase. The maximum wall-normal velocity is always higher at the leading edge and increases with the AOA. As AOA increases the angle of the shear layer increases more than the difference in AOA indicating a difference in the separation bubble. In-plane TKE and streamwise fluctuations extend downstream with the AOA. Wall-normal fluctuations increase with AOA and have similar magnitude at AOA 12°, AOA 13.5° and least at 10.5°.

As the Reynolds number increases, the boundary layer thickness decreases slightly. The wall-normal velocities don't change much with the Reynolds numbers. Reynolds shear stresses are similar in magnitudes at Re = 10^6 and Re =1.48×10^6. The in-plane TKE and streamwise fluctuations are also similar at Re = 10^6 and Re = 1.48×10^6, with the least at Re = 5×10^5. Wall-normal fluctuations are increasing with the Reynolds number and are maximum at the downstream.

In the top-down orientation, the flow statistics don't vary much with changing Reynolds numbers. The reverse flow in the separated region is higher at Re = 5×10^5 than at Re = 10^6. They have similar overall flow separation, Reynolds shear stresses, in-plane TKE, streamwise fluctuations and spanwise fluctuations. In the regions of bad vectors, we can improve the data quality by increasing the signal-to-noise ratio, reducing the effect of reflection from surfaces and cleaning the regions of possible accumulation of high-density particles.

Overall the change across the Reynolds numbers is less than the changes with AOA. The separation is slightly smaller at increased Re, which is more clear in the side-on view than the top-down view.

BIBLIOGRAPHY

[1] Owen Williams Alessandro Pulimeno, Ganesh Bommavaram. Exploration of stall dynamics on a high-speed crm wing. 2024.

[2] Hariprasad Annamalai. Detailed characterization of turbulent separated flow dynamics and boundary layer evolution over a speed-bump geometry. 2022.

[3] Adam M. Clark, Jeffrey P. Slotnick, Nigel Taylor, and Christopher L. Rumsey. Requirements and challenges for cfd validation within the high-lift common research model ecosystem. *AIAA SciTech 2020 Forum*, 2020.

[4] Anthony J. Sclafani Doug S. Lacy. Development of the high lift common research model (hl-crm): A representative high lift configuration for transonic transports. In *AIAA SciTech 2016*, 2016.

[5] J. A. Hannon, A. E. Washburn, L. N. Jenkins, and R. D. Watson. Trapezoidal wing experimental repeatability and velocity profiles in the 14- by 22-foot subsonic tunnel (invited). In *AIAA Paper*, number 0706, January 2012.

[6] Y. Ito, M. Murayama, Y. Yokokawa, K. Yamamoto, K. Tanaka, T. Hirai, H. Yasuda, A. Tajima, and A. Ochi. Jaxa's and khi's contribution to the third high lift prediction workshop. *Journal of Aircraft*, 56(3):1080–1098, 2019.

[7] Owen Williams Chris Morton Kevin H. Manohar, Hariprasad Annamalai and Robert J. Martinuzzi. Unsteadiness in turbulent separated flow over a three-dimensional gaussian hill. *Journal of Fluid Mechanics*.

[8] Seigo Koga, Masataka Kohzai, Makoto Ueno, Kazuyuki Nakakita, and Norikazu Sudani. Analysis of NASA common research model dynamic data in JAXA wind tunnel tests. *AIAA SciTech 2013*.

[9] D. S. Lacy and A. J. Sclafani. Development of the high lift common research model (hl-crm): A representative high lift configuration for transonic transports. In *AIAA Paper 2016-0308*, January 2016.

[10] LaVision. Imager scmos camera data sheet. March 2018.

[11] Jürgen Quest Melissa B. Rivers and Ralf Rudnik. Comparison of the nasa common research model european transonic wind tunnel test data to nasa test data. In *AIAA SciTech Forum*, 2015.

[12] Miguel Salguero, Kirsten Wind Tunnel. Kwt sidewall balance technical guide.

[13] R. Rudnik, K. Huber, and S. Melber-Wilkending. Eurolift test case description for the 2nd high lift prediction workshop. In *AIAA Paper 2012-2924*, June 2012.

[14] C. L. Rumsey and J. P. Slotnick. Overview and summary of the second aiaa high-lift prediction workshop. *Journal of Aircraft*, 52(4):1006–1025, 2015.

[15] C. L. Rumsey, J. P. Slotnick, M. Long, R. A. Stuever, and T. R. Wayman. Summary of the first aiaa cfd high-lift prediction workshop. *Journal of Aircraft*, 48(6):2068–2079, 2011.

[16] C. L. Rumsey, J. P. Slotnick, and A. J. Sclafani. Overview and summary of the third aiaa high-lift prediction workshop. *Journal of Aircraft*, 56(2):621–644, 2019.

[17] M. C. Samuell. Development of a turbulent separated flow validation test case: Experimental and computational (rans) studies. Master's thesis, University of Washington, 2020.

[18] J. Slotnick et al. Vision 2030 cfd study: A path to revolutionary computational aerosciences. Tech. Rep. NASA/CR-2014-218178, NASA, 2014.

[19] Andrew W. Cary John A. Schaefer Vincent Lee Robert Malecki Gorazd Medic Juan J. Alonso Dimitri Mavriplis Timothy M. Mauery, Jeffrey P. Slotnick. A 20-year vision for flight and engine certification by analysis. *AIAA SciTech 2020 Forum*, 2020.

[20] University of Washington, Department of Aeronautics and Astronautics. Kwt technical guide. https://www.aa.washington.edu/AERL/KWT/techguide.

[21] John Vassberg, Mark Dehaan, Melissa Rivers, and Richard Wahls. Development of a common research model for applied cfd validation studies. In *26th AIAA applied aerodynamics conference*, page 6919, 2008.

[22] Francis De Voogt and Bharathram Ganapathisubramani. Effects of a trailing-edge flap on stall cell characteristics of a NACA0012 wing. Cambridge University Press, pages E15-5 & E15-6.

[23] J. Westerweel and F. Scarano. Universal outlier detection for piv data. *Exp. Fluids*, 39(6):1096–1100, 2005.

[24] O. J. Williams, M. Samuell, M. L. Robbins, H. Annamalai, and A. Ferrante. Characterization of separated flowfield over gaussian speed-bump cfd validation geometry. In *AIAA SciTech Forum 2021*.

[25] O. J. Williams, M. Samuell, S. Sarwas, M. L. Robbins, and A. Ferrante. Experimental study of a cfd validation test case for turbulent separated flows. In *AIAA SciTech Forum 2020*.

[26] Owen Williams, Madeline Samuell, Sage Sarwas, Matthew Robbins, and Antonino Ferrante. Experimental study of a cfd validation test case for turbulent separated flows. In *SciTech 2020*, Seattle, WA, U.S.A., 2020. American Institute of Aeronautics and Astronautics.